Astronomy & Astrophysics

The Carnegie Supernova Project II

Observations of the intermediate-luminosity red transient SNhunt120[⋆,⋆⋆]

M. D. Stritzinger[1], F. Taddia[1], M. Fraser[2], T. M. Tauris[3,1], N. B. Suntzeff[4,5], C. Contreras[1,6], S. Drybye[1,7],
L. Galbany[8], S. Holmbo[1], N. Morrell[6], M. M. Phillips[6], J. L. Prieto[9,10], J. Anais[6], C. Ashall[11], E. Baron[12],
C. R. Burns[13], P. Hoeflich[11], E. Y. Hsiao[11], E. Karamehmetoglu[1], T. J. Moriya[14,15], M. T. Botticella[16], A. Campillay[6],
S. Castellón[6], C. González[6], M. L. Pumo[17,18,19], and S. Torres-Robledo[20,6]

[1] Department of Physics and Astronomy, Aarhus University, Ny Munkegade 120, 8000 Aarhus C, Denmark
   e-mail: max@phys.au.dk
[2] School of Physics, O'Brien Centre for Science North, University College Dublin, Belfield, Dublin 4, Ireland
[3] Aarhus Institute of Advanced Studies (AIAS), Aarhus University, Høegh-Guldbergs Gade 6B, 8000 Aarhus C, Denmark
[4] The George P. and Cynthia Woods Mitchell Institute for Fundamental Physics and Astronomy, Texas A&M University,
   College Station, TX 877843, USA
[5] Department of Physics and Astronomy, Texas A&M University, College Station, TX 77843, USA
[6] Las Campanas Observatory, Carnegie Observatories, Casilla 601, La Serena, Chile
[7] Nordic Optical Telescope, Apartado 474, 38700 Santa Cruz de La Palma, Spain
[8] Departamento de Física Teórica y del Cosmos, Universidad de Granada, 18071 Granada, Spain
[9] Núcleo de Astronomía de la Facultad de Ingeniería y Ciencias, Universidad Diego Portales, Av. Ejército 441, Santiago, Chile
[10] Millennium Institute of Astrophysics, Santiago, Chile
[11] Department of Physics, Florida State University, Tallahassee, FL 32306, USA
[12] Homer L. Dodge Department of Physics and Astronomy, University of Oklahoma, 440 W. Brooks, Rm 100, Norman,
   OK 73019-2061, USA
[13] Observatories of the Carnegie Institution for Science, 813 Santa Barbara St, Pasadena, CA 91101, USA
[14] National Astronomical Observatory of Japan, National Institutes of Natural Sciences, 2-21-1 Osawa, Mitaka,
   Tokyo 181-8588, Japan
[15] School of Physics and Astronomy, Faculty of Science, Monash University, Clayton, VIC 3800, Australia
[16] INAF – Osservatorio Astronomico di Capodimonte, Salita Moiarello 16, Napoli, Italy
[17] Università degli studi di Catania, Dip. di Fisica e Astronomia "E. Majorana", Via Santa Sofia 64, 95123 Catania, Italy
[18] INAF – Osservatorio Astronomico di Padova, Vicolo dell'Osservatorio 5, 35122 Padova, Italy
[19] Laboratori Nazionali del Sud-INFN, Via Santa Sofia 62, 95123 Catania, Italy
[20] SOAR Telescope, La Serena 1700000, Chile

ABSTRACT

We present multiwavelength observations of two gap transients that were followed by the Carnegie Supernova Project-II. The observations are supplemented with data obtained by a number of different programs. Here in the first of two papers, we focus on the intermediate-luminosity red transient (ILRT) designated SNhunt120, while in a companion paper we examine the luminous red novae AT 2014ej. Our data set for SNhunt120 consists of an early optical discovery, estimated to be within three days after outburst, the subsequent optical and near-infrared broadband followup extending over a period of about two months, two visual and two near-infrared wavelength spectra, and *Spitzer* Space Telescope observations extending from early (+28 d) to late (+1155 d) phases. SNhunt120 resembles other ILRTs such as NGC 300-2008-OT and SN 2008S, and like these other ILRTs, SNhunt120 exhibits prevalent mid-infrared emission at both early and late phases. From the comparison of SNhunt120 and other ILRTs to electron-capture supernova simulations, we find that the current models underestimate the explosion kinetic energy and thereby produce synthetic light curves that overestimate the luminosity. Finally, examination of pre-outburst *Hubble* Space Telescope images yields no progenitor detection.

Key words. supernovae: individual: SNhunt120 – supernovae: general

1. Introduction

The proliferation of sky surveys over the past decade has driven a dramatic increase in the discovery of transients in the "luminosity gap" between the brightest novae ($M_V \lesssim -10$ mag)

and the faintest classical core-collapse supernovae (SN; peak $M_V \sim -16$ mag). Because they resemble some type IIn supernova, but have a much fainter peak luminosity, these objects have been referred to in the past years as SN imposters (e.g., Schlegel 1990; Filippenko 1997; Van Dyk et al. 2000). However, with the discovery of a low-luminosity subclass of type IIP SNe (e.g., Pastorello et al. 2004) and an ever-increasing diversity of observed phenomena, the SN imposter nomenclature has now become obsolete, and today, SN imposters are typically


⋆ This paper includes data gathered with the 6.5 m *Magellan* telescopes at Las Campanas Observatory, Chile.
⋆⋆ Photometry and spectra presented in this paper are available on WISeREP.
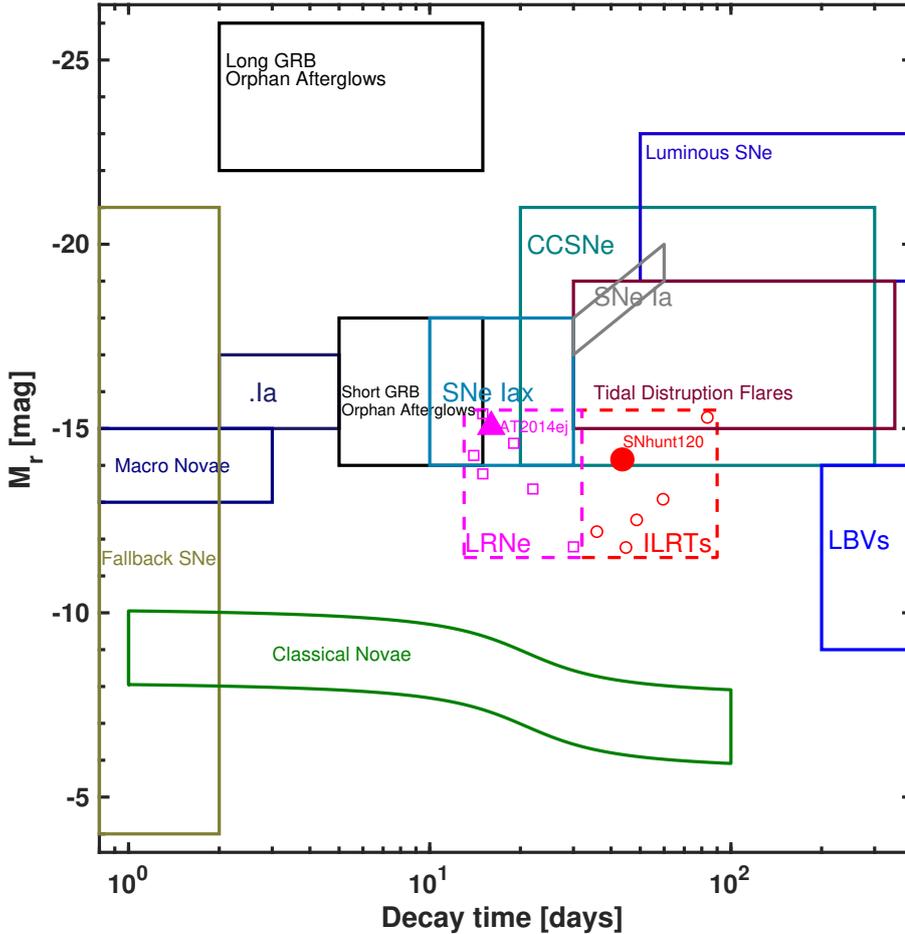
Fig. 1. Absolute peak *r*-band magnitude vs. decay time (defined as the time taken for the *r*-band light curve to decline one magnitude from peak) for optical transients. The figure is adapted from Kasliwal (2011) and Rau et al. (2009). Peak absolute *r*-band magnitudes and decay times for the ILRTs and LRNe are plotted as red circles and magenta squares, respectively. The LRN AT 2014ej plotted as a magenta triangle is a lower limit (see Paper II). The LRNe and ILRTs regions are plotted as dashed lines to highlight the point that the full extent of the parameter space occupied by each subtype is unknown.

associated with luminous blue variables (LBVs; e.g. Smith et al. 2011). Gap transients have also been referred to as intermediate-luminosity optical transients (ILOTs), but we choose not to use this term to avoid confusion with intermediate-luminosity red transients (ILRTs; e.g. Bond et al. 2009), as well as with luminous red novae (LRNe; e.g. Blagorodnova et al. 2017). The early spectra of gap transients are often dominated by Balmer emission lines, typically with full width at half-maximum (FWHM) emission line velocities ranging from $\gtrsim$200–300 km s^{-1} to $\gtrsim$1000 km s^{-1}. This can be taken as evidence for the presence of a preexisting circumstellar medium (CSM) around the progenitor of these transients.

Evidence now indicates that different observational subtypes of gap transients are linked to different progenitors (see Kulkarni et al. 2009; Kochanek et al. 2012a; Kashi & Soker 2016; Pastorello & Fraser 2019, for concise reviews). In Fig. 1 the regions within the peak absolute magnitude versus decay-time parameter space that harbor the different flavors of gap transients are indicated, including LBVs, ILRTs, and LRNe. The figure also includes regions of other known transient populations. LBVs are stars that undergo giant eruptions and display erratic variability that in some cases may occur immediately prior to a star exploding as a core-collapse supernova. ILRTs are commonly linked to super asymptotic giant branch (S-AGB) stars (Prieto et al. 2008, 2009; Thompson et al. 2009; Botticella et al. 2009; Kochanek 2011; Adams et al. 2016; Doherty et al. 2017) that undergo a weak terminal explosion induced by an electron-capture collapse (Miyaji et al. 1980; Nomoto 1984; Miyaji & Nomoto 1987; Hashimoto et al. 1993; Kitaura et al. 2006; Poelarends et al. 2008). Other models have also been presented

to account for ILRTs. For example, it has been proposed that ILRTs are associated with moderately massive ($\sim$20 $M_\odot$) stars embedded in a dusty environment that experience outbursts driven by super-Eddington winds (e.g., Smith et al. 2009; Humphreys et al. 2011). Alternatively, Kashi et al. (2010) presented a model for ILRTs being powered by the gravitational energy release following the accretion of matter from an AGB star onto a main-sequence or more compact companion.

Finally, LRNe may be linked to massive contact binary systems (e.g., Blagorodnova et al. 2017) that undergo a common-envelope ejection while the two stars merge (Smith et al. 2016; Lipunov et al. 2017; Mauerhan et al. 2018). This scenario is the massive star version of common-envelope ejections associated with less massive stars producing red novae with double-peak light curves. Today it remains a matter of open debate whether the merger process driving LRNe culminates in the coalesce of a single star, a weak SN explosion, or even both, depending on the masses and pre-SN mass-loss histories (see Pastorello et al. 2019, for a detailed discussion).

Only a relatively small number of gap transients have been studied in the literature, therefore we present in two papers a detailed study of two gap transients observed by the Carnegie Supernova Project (CSP-II; Phillips et al. 2019). These objects, designated SNhunt120 and AT 2014ej, are both plotted in Fig. 1 along with the handful of other well-observed LRNe and ILRTs from the literature. Inspection of the figure reveals that SNhunt120 is located within the ILRT gap transient region, and AT 2014ej is located within the LRNe gap transient region.

Because so many data have been obtained for the two objects and because our analysis is extended, we elected to present our
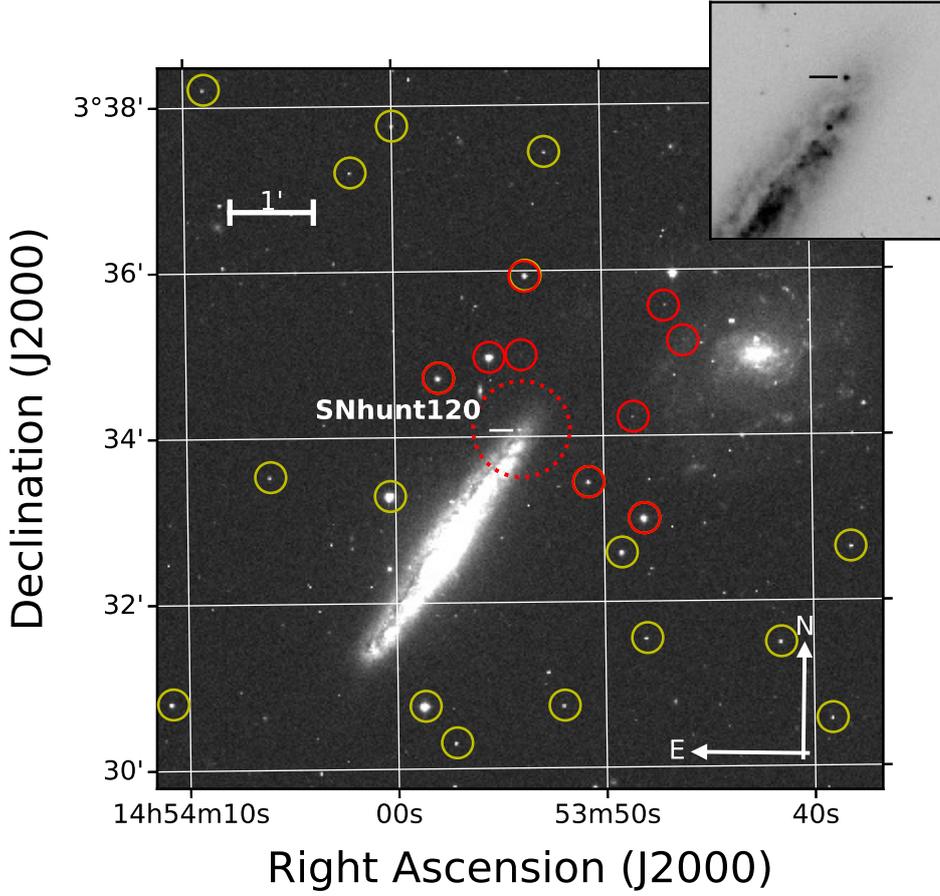
Fig. 2. Finding chart of NGC 5775 hosting SNhunt120 constructed from a single Swope *r*-band image when the transient was near maximum brightness. The position of SNhunt120 is indicated with a dotted circle with a zoom into the area shown in the upper right corner inset. Optical and NIR local sequence stars are indicated with yellow and red circles, respectively.

study of SNhunt120 and AT 2014ej in separate papers. Here in Paper I we focus on SNhunt120, while in the companion paper (Stritzinger et al. 2020; hereafter Paper II) we focus on AT 2014ej. In addition to CSP-II data presented here in Paper I, we also make use of early data obtained by the La Silla-Quest (LSQ) low-redshift supernova survey (Baltay et al. 2013) to estimate the outburst time of SNhunt120. The analysis we present below also makes use of optical photometry previously presented by Bond (2018), two-channel *Spitzer* Space Telescope images spread over 1000 days, and pre-explosion *Hubble* Space Telescope (HST) images of the host galaxy NGC 5775.

2. SNhunt120

2.1. Discovery, distance, and reddening

SNhunt120, also known as PSN J1453595+0334049 and LSQ12brd, was discovered by the Catalina Sky Survey (CSS) on 27.49 March 2012 UT (Howerton et al. 2012) in NGC 5775 with an apparent *V*-band magnitude $m_V = 18.7$ mag. The transient was not detected in CSS images taken on 17.39 March 2012 UT down to a limiting magnitude $m_V > 19.5$. We have also recovered the transient in an LSQ image obtained on 27.30 March 2012 UT with an apparent *gr*-band magnitude of 18.95.

A spectrum obtained on 28.16 March 2012 UT with the 2.5 m du Pont (+WFCCD) telescope at Las Campanas Observatory (LCO), reported by Howerton et al. (2012), exhibits Balmer emission lines and both allowed and forbidden Ca II features. Furthermore, the Hβ λ4861 and Hα λ6563 Balmer lines are characterized by FWHM velocities of $v_{FWHM} \sim 650$ km s^{-1}. These characteristics, along with the fact that the transient reached an absolute *V*-band magnitude $M_V \approx -13.9$ mag, led Howerton

et al. (2012) to identify it as a possible gap transient similar to SN 2008S (Botticella et al. 2009) and NGC 300-2008-OT (Bond et al. 2009; Humphreys et al. 2011).

Berger et al. (2012) reported on the possible detection of a source at the position of this gap transient in a pre-explosion archival HST (+ ACS/F625W) image of NGC 5775, measuring an apparent magnitude of 25.5–26, and provided corresponding absolute magnitudes of ∼−6.1 to −6.6, assuming a distance of 31 Mpc. This is larger than the value we adopt. For our distance value (see below), the absolute magnitude would be between −4.7 and −5.2 mag.

With J2000 coordinates of $\alpha = 14^h53^m53\overset{s}{.}95$ and $\delta = +03°34'04\overset{''}{.}9$, SNhunt120 was located 55″ west and 85″ north from the core of its host NGC 5775 (see Fig. 2 for a finding chart). NGC 5775 is an edge-on SBc spiral galaxy and is a member of the Virgo cluster. The NASA/IPAC Extragalactic Database (NED)[1] lists its heliocentric redshift as $z = 0.005607$ and also lists over half a dozen different Tully-Fisher distances from the literature, ranging from 15.9 to 27.0 Mpc (distance moduli from 31.0 ± 0.40 mag to 32.15 ± 0.40 mag). However, as NGC 5775 is a member of the Virgo cluster, we opt to use the more precise distance modulus to Virgo of $\mu = 31.03 \pm 0.14$ mag, which is based on a Cepheid calibration of the Tully-Fisher relation as presented by Tully et al. (2016).

In Appendix A we compute the host redshift and metallicity using a spectrum of NGC 5775 obtained by the Sloan Digital Sky Survey, while Appendix B contains details on the Galactic reddening in the direction of SNhunt120 and our estimate of its host-galaxy reddening. In short, in the work presented below, we adopted a total visual extinction of $A_V^{tot} = 0.76 \pm 0.25$ mag.

---

[1] http://ned.ipac.caltech.edu

Table 1. Photometry of the local sequence for SNhunt120 in the "standard" system.

ID	α (2000)	δ (2000)	B	V	u'	g'	r'	i'
1	223.501175	3.554772	...	...	...	...	...	...
2	223.494568	3.512511	...	...	...	...	...	...
3	223.450409	3.549971	...	...	...	...	...	...
4	223.491287	3.578468	16.572(028)	16.018(011)	17.253(048)	16.239(009)	15.847(019)	15.692(010)
5	223.454926	3.543110	16.771(020)	16.082(012)	17.797(071)	16.387(010)	15.892(007)	15.716(010)
6	223.473694	3.598971	17.385(050)	16.734(025)	18.245(055)	17.016(035)	16.567(029)	16.392(021)
7	223.545074	3.513310	17.712(029)	17.034(024)	18.675(033)	17.374(035)	16.854(013)	16.661(024)
8	223.423279	3.524919	18.486(023)	17.988(049)	19.094(043)	18.198(036)	17.827(034)	17.709(060)
9	223.409164	3.544031	18.709(027)	18.131(044)	19.455(207)	18.315(119)	17.930(072)	17.795(068)
10	223.525085	3.558814	19.137(166)	18.274(018)	20.034(082)	18.703(032)	17.994(079)	17.723(096)
11	223.461456	3.557315	19.394(061)	17.967(060)	19.917(172)	18.701(003)	17.397(041)	16.743(016)
12	223.466751	3.512445	19.219(068)	18.595(080)	19.980(066)	18.800(085)	18.276(096)	18.154(070)
13	223.450058	3.525849	19.625(047)	18.460(053)	...	18.985(028)	17.875(043)	17.522(032)
14	223.413147	3.509561	19.529(075)	18.903(025)	19.950(072)	19.241(025)	18.724(024)	18.467(052)
15	223.500031	3.629244	19.735(062)	18.549(084)	...	19.149(033)	17.913(043)	17.394(027)
16	223.488373	3.505094	19.659(061)	18.660(035)	...	19.168(068)	18.195(060)	17.927(074)
17	223.537628	3.636855	19.683(100)	19.045(044)	20.249(094)	19.355(005)	18.847(103)	18.771(035)
18	223.432632	3.621403	19.990(188)	19.316(039)	20.400(132)	19.637(111)	19.189(035)	18.764(062)
19	223.469666	3.623828	19.806(138)	19.236(086)	...	19.574(057)	18.878(003)	18.537(061)
20	223.407272	3.620129	19.984(091)	19.721(097)	19.100(063)	20.079(100)	19.521(052)	19.187(014)
21	223.508453	3.619909	20.646(152)	19.390(189)	...	20.051(112)	18.770(084)	18.039(116)

Notes. Values in parenthesis are 1σ uncertainties that correspond to the rms of the instrumental errors of the photometry obtained over a minimum of three nights observed relative to standard star fields.

2.2. Observations

The CSP-II obtained 22 epochs of *ugriBV*-band images of SNhunt120 with the Swope (+ CCD camera) telescope located at LCO extending between +2 to +46 days (d) past first detection. Two epochs of *YJH*-band NIR photometry were obtained with the du Pont (+ RetroCam; Hamuy et al. 2006) telescope on +16 d and +37 d, while two epochs of *Y*-band photometry were obtained nearly a day apart on +153 d and +154 d. A single *J*-band observation was also obtained a day later. The raw data were reduced using standard CSP-I pipelines as described in detail by Krisciunas et al. (2017) and references therein. Prior to computing photometry, deep host-galaxy template images were subtracted from all of the optical science images, but not for the NIR science images because we lack template images.

Photometry of SNhunt120 was computed relative to a local sequence of stars calibrated with respect to optical and NIR standard star fields observed over a minimum of three photometric nights. The optical photometry of these stars in the "standard" system is presented in Table 1, while NIR photometry of a smaller set of stars in the standard system is given in Table 2. Finally, our optical and NIR photometry of SNhunt120 in the CSP-II "natural" photometric systems are listed in Tables 3 and 4, respectively.

The La Silla Quest (LSQ) survey observed NGC 5775 multiple times over a period of several years, and we are able to identify SNhunt120 in 17 epochs of LSQ *gr*-band imaging. Prior to computing photometry of SNhunt120 from these images, a deep galaxy template image was constructed from a series of 15 LSQ images obtained prior to discovery. After subtracting the template image from the science images, point spread function (PSF) fitting photometry of SNhunt120 was computed relative to the *V*-band magnitude of a single bright star in the field of NGC 5775, which is calibrated by the CSP-II data and designated with the ID of 3 (see below). Following Contreras et al. (2018, see their Fig. 23), PSF photometry was computed from

Table 2. NIR photometry of the local sequences for SNhunt120 in the "standard" system.

ID	α(2000)	δ(2000)	Y	N	J_{rc2}	N	H	N
101	223.4504	3.549965	13.60(01)	4	13.40(34)	5	12.73(03)	5
102	223.4811	3.582550	13.65(02)	5	13.41(03)	6	13.07(02)	6
103	223.4913	3.578437	15.10(02)	5	14.84(03)	6	14.47(03)	6
104	223.4615	3.557310	15.73(04)	5	15.25(04)	6	14.57(04)	6
105	223.4739	3.598759	15.66(04)	1	15.52(03)	2	15.23(06)	1
106	223.4524	3.570402	16.97(10)	4	16.37(15)	5	15.76(10)	5
107	223.4747	3.582985	17.47(21)	3	17.13(20)	3	16.53(19)	3

Notes. Values in parenthesis are 1σ uncertainties and correspond to an rms of the instrumental errors of the photometry obtained over the number of photometric nights N that standard star fields were observed.

the LSQ *gr*-band images and calibrated relative to the Swope natural *V*-band photometric system. The LSQ photometry is listed in Table 5.

A search of the *Spitzer* data archive reveals images were obtained of SNhunt120 over several epochs with the 3.6 μm and 4.5 μm channels. Specifically, the transient was detected during two early epochs (+28 d and +39 d), and also at late times on +1155 d. Fully reduced stacked images were downloaded from the *Spitzer* archive. PSF photometry was computed with a pipeline developed in `Matlab`, and the results are listed in Table 6. These fluxes are used below to construct spectral energy distributions (SEDs) for SNhunt120 extending from the atmospheric cutoff out to 4.5 μm.

Turning to spectroscopy of SNhunt120, two epochs of visual wavelength observations are presented. This includes the classification spectrum and a followup spectrum taken by the CSP-II. These are complemented with two epochs of NIR spectroscopy also obtained by the CSP-II, which to our knowledge represent the first NIR spectra published of an ILRT. A summary

Table 3. Optical photometry of SNhunt120 in the Swope "natural" system.

Time [†]	u	Time [†]	B	Time [†]	g	Time [†]	V	Time [†]	r	Time [†]	i
15.82	19.386(0.026)	15.80	18.823(0.018)	15.82	18.512(0.015)	15.79	18.247(0.017)	15.81	17.990(0.014)	15.81	17.814(0.016)
16.84	19.201(0.024)	16.86	18.637(0.014)	16.84	18.311(0.011)	16.87	18.062(0.013)	16.85	17.835(0.011)	16.85	17.665(0.013)
17.77	19.068(0.025)	17.75	18.519(0.016)	17.78	18.195(0.013)	17.74	17.972(0.016)	17.76	17.731(0.011)	17.76	17.587(0.017)
19.84	18.875(0.022)	19.85	18.345(0.013)	19.83	18.060(0.009)	19.86	17.855(0.011)	19.83	17.637(0.009)	19.84	17.510(0.009)
20.82	18.810(0.104)	20.80	18.293(0.013)	20.82	18.025(0.009)	20.81	17.820(0.010)	20.83	17.605(0.011)	20.84	17.496(0.010)
21.88	18.786(0.020)	21.84	18.256(0.010)	21.86	17.993(0.008)	21.85	17.808(0.010)	21.86	17.605(0.009)	21.87	17.468(0.009)
22.86	18.752(0.032)	22.84	18.279(0.016)	22.87	17.986(0.010)	22.83	17.792(0.011)	22.86	17.590(0.009)	22.85	17.476(0.009)
23.77	18.773(0.036)	23.75	18.273(0.020)	23.77	17.973(0.013)	23.74	17.794(0.015)	23.76	17.577(0.014)	23.76	17.455(0.015)
24.68	18.730(0.057)	24.69	18.255(0.027)	24.67	17.983(0.018)	24.70	17.800(0.018)	24.68	17.564(0.013)	24.69	17.490(0.013)
25.85	18.846(0.069)	25.83	18.274(0.026)	25.85	17.997(0.019)	25.82	17.774(0.017)	25.84	17.589(0.012)	25.84	17.493(0.012)
28.83	18.846(0.031)	28.80	18.293(0.013)	28.82	18.054(0.011)	28.81	17.865(0.013)	28.82	17.678(0.011)	28.83	17.557(0.009)
. . .	. . .	29.80	18.349(0.014)	29.81	18.086(0.010)	29.81	17.904(0.010)	29.83	17.686(0.009)	29.84	17.567(0.010)
34.89	19.151(0.030)	34.87	18.549(0.015)	34.90	18.253(0.010)	34.87	18.057(0.011)	34.89	17.868(0.011)	34.88	17.766(0.011)
35.77	19.153(0.024)	35.75	18.558(0.017)	35.78	18.285(0.012)	35.74	18.090(0.014)	35.77	17.908(0.012)	35.76	17.781(0.014)
36.79	19.209(0.028)	36.77	18.603(0.014)	36.80	18.323(0.011)	36.77	18.138(0.012)	36.79	17.950(0.010)	36.78	17.834(0.014)
37.84	19.244(0.026)	37.82	18.646(0.014)	37.84	18.377(0.010)	37.81	18.179(0.012)	37.83	17.967(0.010)	37.82	17.852(0.011)
47.87	19.871(0.067)	47.85	19.078(0.019)	47.88	18.745(0.014)	47.84	18.459(0.013)	47.86	18.248(0.012)	47.86	18.089(0.014)
50.78	20.125(0.086)	50.76	19.230(0.030)	50.79	18.882(0.020)	50.75	18.546(0.021)	50.77	18.289(0.012)	50.77	18.076(0.015)
. . .	. . .	52.75	19.363(0.042)	52.77	18.904(0.023)	52.76	18.629(0.025)	52.78	18.323(0.015)	52.79	18.129(0.015)
53.74	20.105(0.142)	53.70	19.264(0.045)	53.72	18.912(0.027)	53.71	18.646(0.026)	53.73	18.343(0.015)	53.73	18.140(0.016)
55.76	20.394(0.139)	55.78	19.360(0.059)	55.74	19.002(0.030)	55.77	18.682(0.030)	55.75	18.379(0.022)	55.73	18.115(0.026)
59.77	20.773(0.133)	59.79	19.638(0.039)	59.78	19.114(0.016)	59.79	18.782(0.019)	59.78	18.449(0.013)	59.76	18.179(0.014)

Notes. Values in parenthesis are 1-σ uncertainties corresponding to the sum in quadrature of the instrumental error and the nightly zero-point error.
[†]JD+2456000.

Table 4. NIR photometric observations of SNhunt120 in the du Pont (+ RetroCam) "natural" system.

JD	Photometry [mag]	Error [mag]	Filter [mag]
2456029.82	17.21	0.02	Y
2456050.74	17.68	0.01	Y
2456050.75	17.70	0.01	Y
2456029.87	16.85	0.02	J_{rc2}
2456050.78	17.22	0.02	J_{rc2}
2456050.79	17.20	0.02	J_{rc2}
2456029.85	16.50	0.02	H
2456050.77	16.75	0.03	H
2456050.77	16.76	0.03	H

Notes. The uncertainties in photometry correspond to the sum in quadrature of the instrumental error and the nightly zero-point error.

Table 5. LSQ gr-band photometry of SNhunt120 in the Swope "natural" system.

JD	V [a]	Err
2456013.80	18.951	0.054
2456014.80	18.678	0.108
2456017.79	18.042	0.010
2456018.79	18.001	0.060
2456021.78	17.873	0.017
2456022.78	17.858	0.019
2456024.70	17.850	0.100
2456032.73	18.085	0.012
2456034.85	18.144	0.013
2456036.71	18.237	0.036
2456040.70	18.332	0.019
2456048.62	18.545	0.022
2456050.66	18.511	0.057
2456057.57	18.573	0.140
2456071.50	19.035	0.049
2456075.53	19.377	0.082
2456079.51	19.264	0.079

Notes. [a]Photometry is computed relative to the V-band magnitude of star with identification (ID) number 3 in Table 1. To facilities good agreement between the LSQ gr-band and CSP-II V-band light curves, a 0.03 mag offset was added to the CSP-II magnitude of star 3 as explained in the text.

of these observations is provided in the log of spectroscopic observations in Table 7. The visual wavelength spectra were obtained with the du Pont (+ WFCCD) telescope on +0.9 d and +35.7 d post discovery, while the NIR spectra were taken with the *Magellan* Baade (+ FIRE) telescope on +11.9 d and +40.7 d. The optical data were reduced following standard methods as described in Hamuy et al. (2006) and Krisciunas et al. (2017) and the NIR reductions following the prescription of Hsiao et al. (2019).

3. Results

3.1. Photometry, explosion epoch, intrinsic broadband colors, and spectral energy distributions

First we examine the discovery and early followup photometry of SNhunt120 obtained by CSP-II, LSQ, CSS, and Bond (2018) and plotted in Fig. 3. Overplotted on the photometry is the best-fit power-law function fit to the first six epochs of obser-

vations, characterized by a power-law index of $\alpha = 0.57 \pm 0.20$. Extrapolating to zero flux provides an explosion epoch on JD–2456012.58 ± 0.95, which is 1.25 days prior to the first LSQ detection.

Now we proceed to examine the full set of broadband photometry obtained for SNhunt120. Optical ($ugriBV$) and NIR (YJH) light curves of SNhunt120 are plotted in Fig. 4. The

Table 6. *Spitzer* fluxes for SNhunt120.

MJD	3.6 μm	4.5 μm
56041.24	$5.60 \times 10^{-18} \pm 2.66 \times 10^{-20}$	$3.61 \times 10^{-18} \pm 2.19 \times 10^{-20}$
56052.83	$4.95 \times 10^{-18} \pm 2.68 \times 10^{-20}$	$3.30 \times 10^{-18} \pm 2.08 \times 10^{-20}$
57168.52	$8.90 \times 10^{-19} \pm 1.68 \times 10^{-19}$	$1.18 \times 10^{-18} \pm 7.73 \times 10^{-21}$

Notes. Fluxes in erg s^{-1} Å^{-1} cm^{-2}.

Table 7. Journal of Spectroscopic Observations of SNhunt120.

Object	Date (JD)	Date (UT)	Days since discovery [a]	Telescope	Instrument	Resolution (Å)
SNhunt120	2456014.66	March 28.16	+0.7	du Pont	WFCCD	7.5
SNhunt120	2456025.79	April 08.29	+11.8	Baade	FIRE	22
SNhunt120	2456049.65	May 02.15	+35.7	du Pont	WFCCD	7.5
SNhunt120	2456054.75	May 07.25	+40.8	Baade	FIRE	22

Notes. [a]Days since outburst assuming outburst date of 25.15 March 2012 UT (JD-2456011.7).
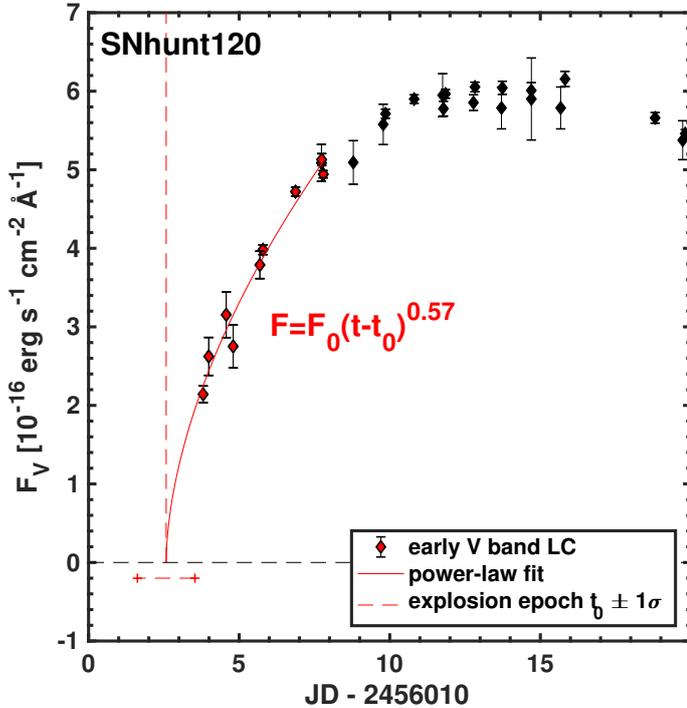
Fig. 3. Early light curve of SNhunt120 plotted with a best-fit power-law function (solid line, reduced $\chi^2 = 4.6$) to the first ten epochs (red points) of photometry. The explosion epoch, t_0, is estimated to have occurred on JD$+2456012.58 \pm 0.95$, which is 1.25 days prior to the first-detection epoch. The dashed red line marks t_0 as obtained from the fit, its uncertainty is marked by a red segment just below the zero-flux level.

optical light curves of SNhunt120 exhibit a ∼0.5 mag rise to maximum over the first week of evolution covered by our observations. Upon reaching maximum, the optical light curves declined by ≈1.0 mag over the period of a month.

At maximum, SNhunt120 reached an apparent magnitude of $m_V = 17.78 \pm 0.01$ mag, which when corrected for the adopted extinction using a standard reddening law and distance corresponds to an absolute magnitude of $M_V = -14.03 \pm 0.29$ mag. Here the accompanying uncertainty is computed by adding in quadrature the uncertainties on A_V^{host} and on the adopted distance.
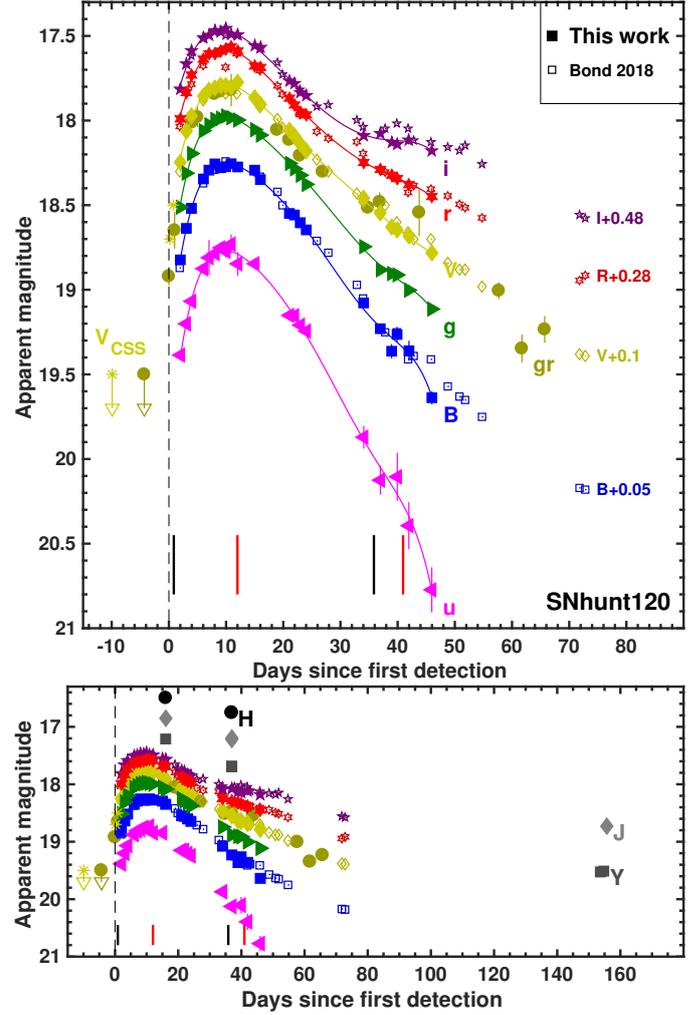
Fig. 4. *Top*: optical *uBgVri*-band photometry of SNhunt120 obtained by the CSP-II and *gr*-band photometry from LSQ. The light curves cover the rise to maximum and subsequent decline over the period of a month and a half. The Catalina Sky Survey (CSS; Howerton et al. 2012) reported *V*-band discovery magnitude of 18.7 obtained on March 27.49, a CSS *V*-band nondetection limit of 19.5 mag obtained from data taken on March 17.39 UT, and an unfiltered photometry point obtained on March 28.07 of 18.5 mag are also plotted. The *BVRI* photometry published by Bond (2018) is overplotted with open symbols; each band is shifted by arbitrary constants to match their most similar CSP-II band. The CSP-II light curves are fit with low-order polynomials plotted as solid colored lines. Optical spectral phases are marked by black segments, and NIR spectral phases are marked by red segments. *Bottom*: as in the top panel, but also including the NIR (*YJH*) points of SNhunt120.

A summary of peak apparent and absolute peak magnitudes for each of the optical bands is listed in Table 8. The peaks were obtained by fitting low-order polynomials to the light curves, and these polynomials are plotted in Fig. 4. Because the reddening estimate is uncertain, peak magnitudes are listed with and without host-reddening corrections. Inspection of the values listed in Table 8 indicates that the optical light curves all peaked within a day of each other and that the various peak absolute magnitudes exhibit ∼0.7 mag in scatter, with the *u* band being the faintest (i.e., $M_u = -13.43 \pm 0.29$ mag) and the *r* band the brightest (i.e., $M_r = -14.12 \pm 0.29$ mag).

We plot in Fig. 5 the intrinsic $(B - V)_0$, $(V - r)_0$, and $(r - i)_0$ broadband colors of SNhunt120. Also shown are the intrinsic broadband colors of the well-observed ILRTs

Table 8. Phase and value of peak absolute magnitudes of SNhunt120.

Band X	Phase[(*)]	m_X	M_X	Reddening corrected M_X
u	9.72 ± 0.4	18.77 ± 0.01	-13.58 ± 0.14	-13.43 ± 0.29
B	10.00 ± 0.2	18.25 ± 0.01	-14.09 ± 0.14	-13.80 ± 0.29
g	9.62 ± 0.2	17.98 ± 0.01	-14.37 ± 0.14	-13.98 ± 0.29
V	9.59 ± 0.2	17.78 ± 0.01	-14.56 ± 0.14	-14.03 ± 0.29
r	9.41 ± 0.2	17.57 ± 0.01	-14.77 ± 0.14	-14.12 ± 0.29
i	9.11 ± 0.2	17.46 ± 0.01	-14.88 ± 0.14	-14.07 ± 0.29

Notes. [(*)]Days since first detection.

M85-2006-OT1 (Kulkarni et al. 2007; Pastorello et al. 2007), SN 2008S (Botticella et al. 2009), NGC 300-2008-OT1 (Bond et al. 2009), PTF10fqs (Kasliwal et al. 2011), AT 2017be (Cai et al. 2018), and AT 2019abn (Jencson et al. 2019; Williams et al. 2020). The photometry of SNhunt120, M85-OT2006-1, SN 2008S, NGC 300-2008-OT1, PTF10fqs, AT 2017be, and AT 2019abn were corrected for reddening by adopting the $E(B - V)_{\rm tot}$ values listed in Table 9. The host extinction of SNhunt120, as discussed in Appendix B, was assumed to be $A_V^{\rm host} = 0.64$ mag in order to match the color curves of the bluest objects of the comparison sample. Over the first days of evolution, while SNhunt120 increased in brightness, its optical colors evolved toward the blue, and this behavior is most apparent in SNhunt120 (and AT 2017be, but with larger error) among the other ILRTs, whose multiband observations started later than those for SNhunt120 (for NGC 300-2008-OT1 about 20 days after first detection, see Bond et al. 2009). Upon reaching maximum, the colors of SNhunt120 transition and evolve to the red as the object continued to expand and cool. The overall evolution of the ILRTs are similar, but PTF10fqs and M85-2006-OT1 exhibit redder $(r-i)_0$ and/or $(R-I)_0$ colors than the other objects, and the $(B-V)_0$ of AT 2017be is redder than SNhunt120 and the other objects.

We now proceed to use the broadband photometry of SNhunt120 to construct SEDs and then fit them with blackbody (BB) functions, in order to estimate the BB luminosity ($L_{\rm BB}^{\rm hot}$), a BB-radius ($R_{\rm BB}^{\rm hot}$) and BB-temperature ($T_{\rm BB}^{\rm hot}$) evolution over time. To do so, the broadband magnitudes in the Swope natural system were transformed to AB magnitudes (Krisciunas et al. 2017), corrected for extinction, and then converted into monochromatic fluxes at the effective wavelengths of each passband. The resulting SEDs and their corresponding best-fit BB functions are plotted in the left panel of Fig. 6, while the right panels display the temporal evolution (from top to bottom) of $L_{\rm BB}^{\rm hot}$, $T_{\rm BB}^{\rm hot}$, and $R_{\rm BB}^{\rm hot}$. To complement our analysis, SEDs are also plotted (dashed lines) based on photometry published by Bond (2018). To facilitate comparison, the Bond data were shifted to match the CSP-II photometry through the use of a single additive constant for each bandpass.

Inspection of the BB parameter profiles reveals that the $T_{\rm BB}^{\rm hot}$ increases as the light curve rises to peak, with $T_{\rm BB}^{\rm hot}$ reaching a maximum value of ~8700 K. Subsequently, as the luminosity declines, $T_{\rm BB}^{\rm hot}$ also declines, reaching $\lesssim 6000$ K at +50 d, whereupon it follows a plateau. At early times, the BB radius is about 2.0×10^{14} cm and declines until +30 d, whereupon it increases over a three-week period before settling onto a plateau phase. The comparison between the bolometric quantities derived from the CSP-II data (red diamonds) and those from the Bond data (black empty diamonds), reveal the effect of including u band in the SEDs, which is only available in the CSP-II data.
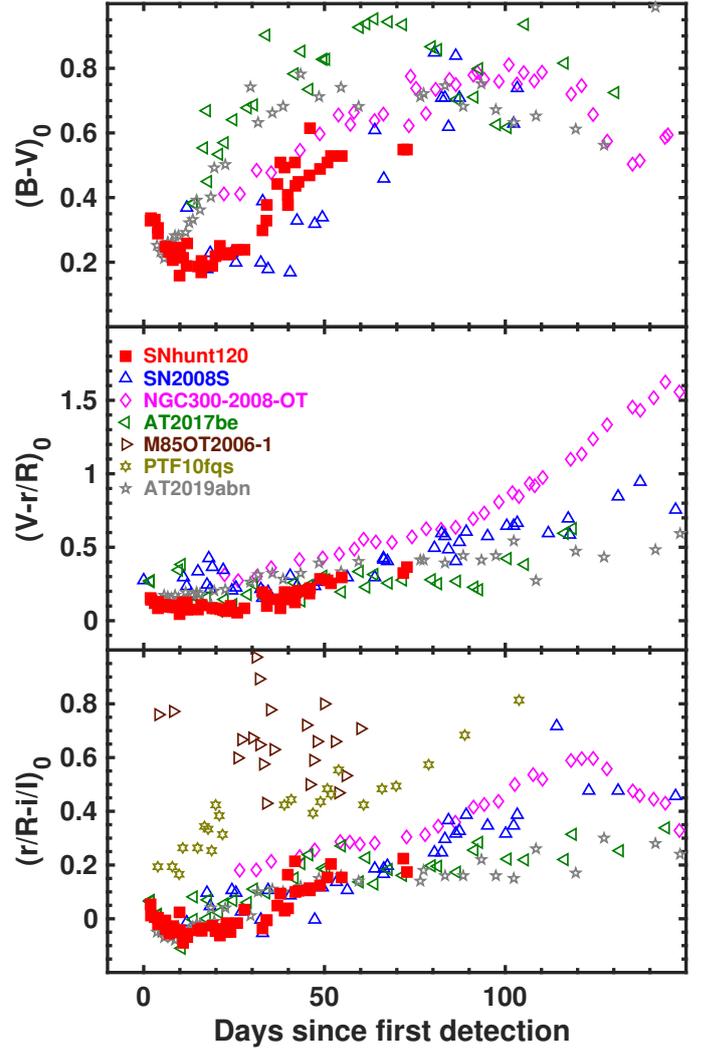

Fig. 5. Intrinsic broadband optical color evolution of SNhunt120 compared to the ILRTs M85-OT2006-1 (Kulkarni et al. 2007; Pastorello et al. 2007), SN 2008S (Botticella et al. 2009), NGC 300-2008-OT1 (Bond et al. 2009), PTF10fqs (Kasliwal et al. 2011), AT 2017be (Cai et al. 2018), and AT 2019abn (Williams et al. 2020). The colors are corrected for reddening adopting the values listed in Sect. 3.1. For SNhunt120, we adopt $A_V^{\rm host} = 0.64$ mag and a Fitzpatrick (1999) reddening law so that its broadband colors match the colors of the bluest objects in the comparison sample.

Table 9. Adopted color excess values and distance moduli for the ILRT sample compared to SNhunt120.

ILRT	μ (mag)	$E(B - V)_{\rm tot}$ (mag)
M85-OT2006-1	31.03	0.14
SN 2008S	31.34	0.69
NGC 300-2008-OT1	28.78	0.40
PTF10fqs	26.37	0.04
AT 2017be	31.15	0.09
AT 2019abn	31.64	0.85

The luminosity is effectively identical, but the temperature is slightly overestimated by ~500–1000 K when the u band is excluded.
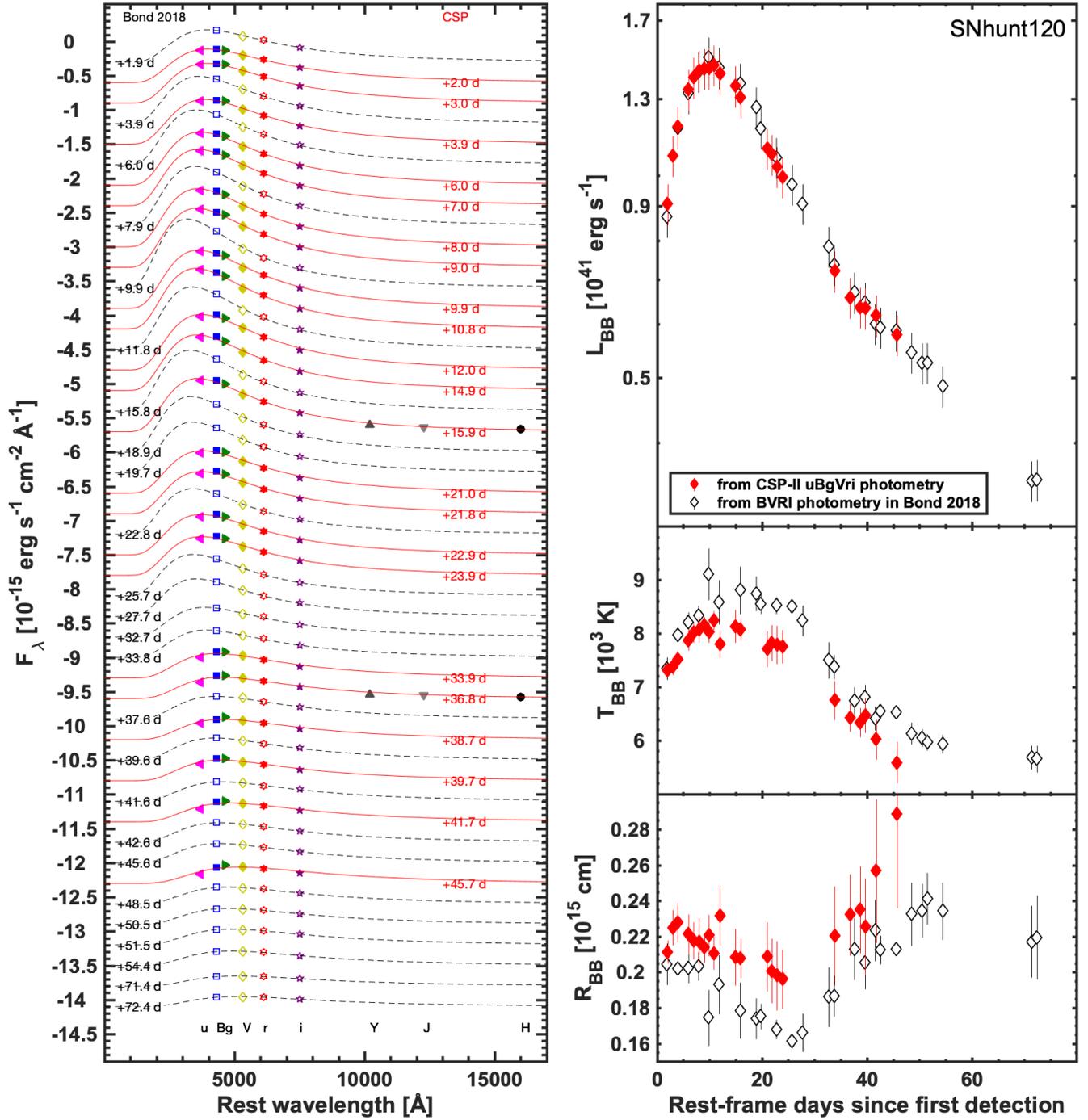
Fig. 6. *Left*: spectral energy distributions of SNhunt120 constructed from our optical photometry and complemented with photometry from Bond (2018). The best-fit BB is overplotted on each SED function; red lines are the fit to CSP-II data, and black lines are the fit to Bond data. For clarity, the SEDs are shifted by arbitrary constants, and the phase of each SED relative to the epoch of discovery is indicated. *Right*: resulting time evolution of the BB luminosity *(top)*, BB temperature *(middle)*, and BB radius *(bottom)* of the underlying emission region corresponding to the BB fits.

Farther redward, beyond the optical and NIR wavelengths, we also consider the two-channel *Spitzer* imaging shown in Fig. 7 (top panel). Through linear interpolation of the corresponding photometry, we obtain a measure of the mid-infrared (MIR) brightness of SNhunt120 on +36.8 d, when photometry is available in all bands. Our early-time extended SED is shown in Fig. 7 (middle panel). Inspection of the SED indicates an MIR excess above the flux reproduced by a single BB fit (blue dashed

line) characterized by the temperature $T_{\mathrm{BB}}^{\mathrm{hot}}$ shown in Fig. 6. This MIR excess can be reproduced by another warm BB component. However, its temperature is characterized by a large uncertainty because the flux of this warm component is far lower than that of the hot component. Finally, in the bottom panel of Fig. 7 we fit the late-phase +1155 d *Spitzer* photometry with a single BB component characterized by $T_{\mathrm{BB}}^{\mathrm{warm}} = 577$ K. We note that there may be legitimate concerns in estimating $T_{\mathrm{BB}}^{\mathrm{warm}}$ and $R_{\mathrm{BB}}^{\mathrm{warm}}$ from BB fits if the underlying SED contained within the wavelength
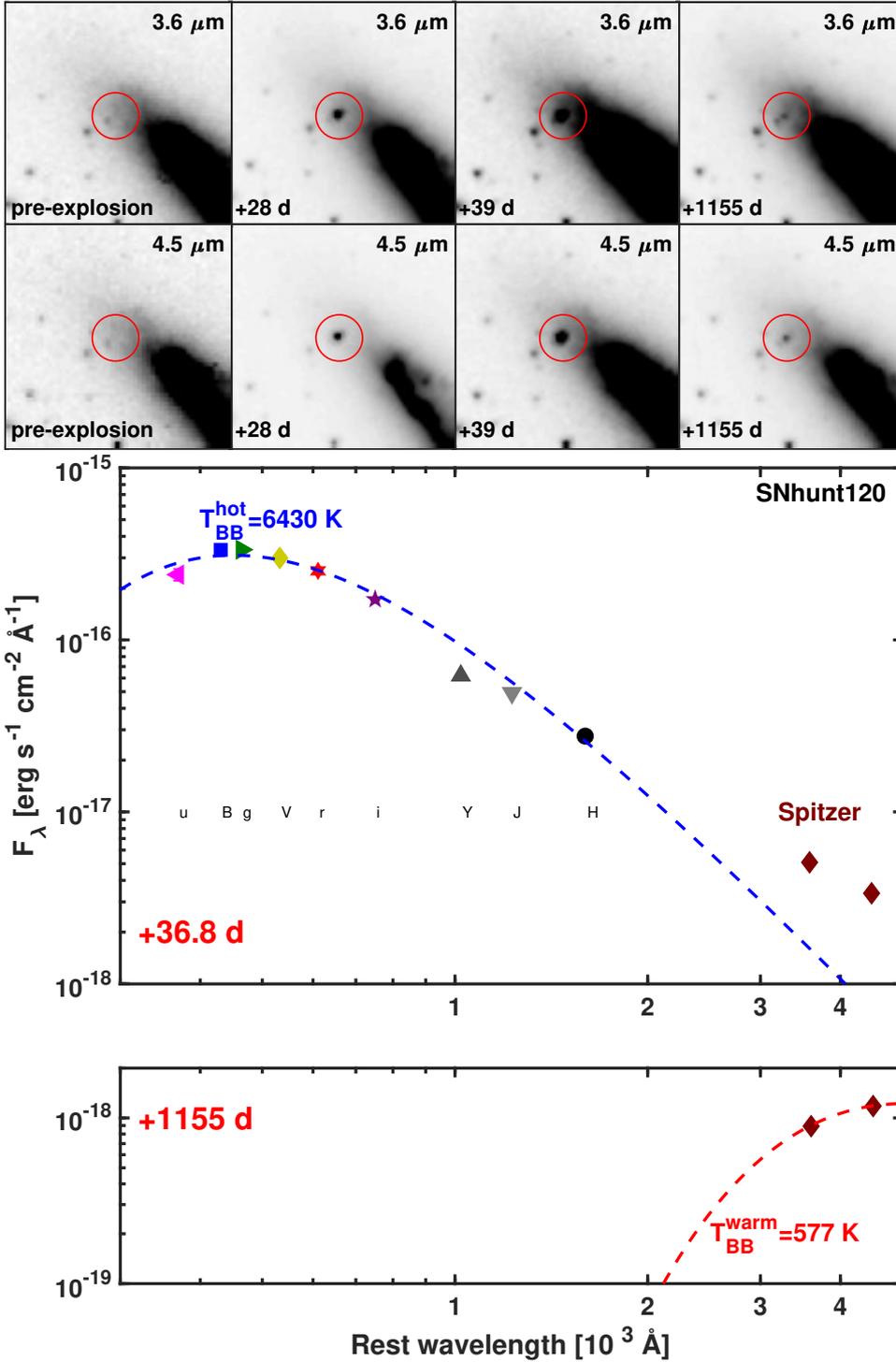
Fig. 7. *Top*: *Spitzer* Space Telescope images of SNhunt120 obtained on +28 d, +39 d, and +1155 d at 3.6 μm and 4.2 μm, the position of the transient is indicated with a red circle. *Bottom*: two-panel plot containing SEDs constructed for SNhunt120 at early and late phases, along with BB fits. The early SED is constructed with CSP-II photometry taken on +36.8 d and *Spitzer* measurements obtained by interpolating between estimated magnitudes obtained from +28 d and +39 d images. A BB function fit (blue dashed line) characterized by a temperature of $T_{\rm BB}^{\rm hot} = 6430 \pm 266$ K is overplotted on the early SED. The BB reproduces the fluxes from *u* to *H* band. However, the *Spitzer* MIR fluxes are clearly above the flux level of the best BB fit, suggesting the presence of an additional cooler component. The SED constructed using the +1155 d *Spitzer* flux points is fit with a BB function characterized by $T_{\rm BB}^{\rm warm} \sim 600$ K.

intervals sampled by the *Spitzer* flux points includes prominent emission or absorption features. However, these concerns are somewhat alleviated when we consider that MIR spectroscopic observations of the ILRT NGC 300-2008-OT published by Ohsawa et al. (2010) revealed an MIR SED consistent with a smooth continuum lacking prominent emission or absorption features.

3.2. Spectroscopy

The two epochs of visual wavelength and NIR spectroscopy of SNhunt120 are plotted in Fig. 8, and their flux calibration was

scaled to be consistent with the observed broadband photometry. The optical spectra consist of a continuum with superimposed Balmer emission lines (Hα, Hβ, and Hγ) and the [Ca II] λλ7291, 7324 doublet. In addition, the spectra exhibit absorption features of Na I *D*, Ca II H&K, and the Ca II NIR triplet. The NIR spectra are to our knowledge the first of an ILRT published to date. These spectra exhibit a handful of prominent features, including emission lines arising from the Paschen series: Pδ, Pγ, and Pβ. In the second NIR spectrum (+41 d), a narrow emission feature emerges just blueward of the Pγ feature, which is likely He I λ10830. None of the features exhibited in these spectra show convincing evidence of P Cygni absorption profiles. The
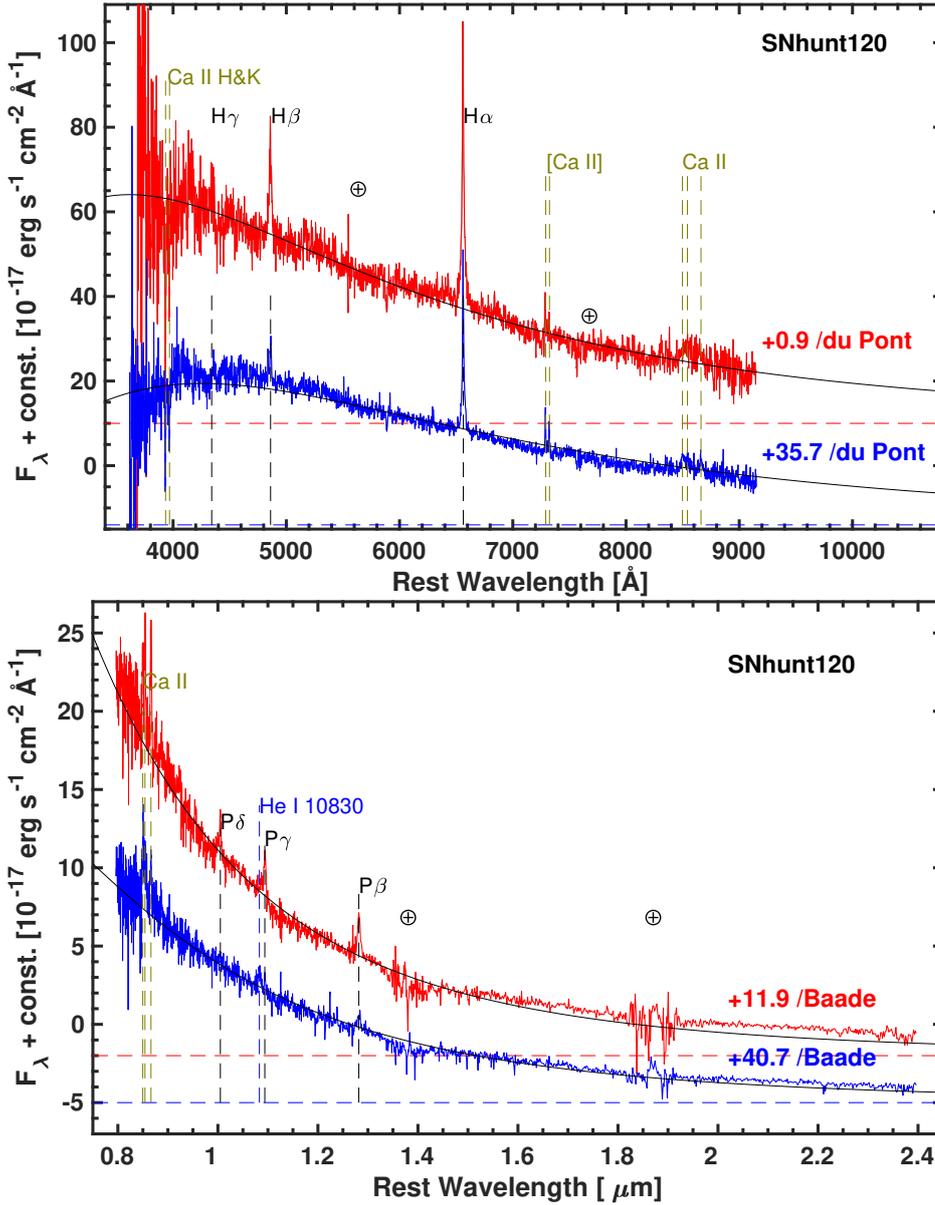
Fig. 8. Low-resolution visual (*top panel*) and NIR wavelength (*bottom panel*) spectra of SNhunt120 in the rest frame. The flux calibration of each spectrum is adjusted to match the corresponding broadband photometry, and the spectra are corrected for both MW and host-galaxy extinction. The spectra are separated for presentation by the addition of an arbitrary constant. Best-fit BB functions are overplotted as black lines, and the phase of each spectrum relative to the discovery epoch and telescope used to obtain the data is indicated.

BB fit to the spectra in the NIR shows a possible excess above $2\,\mu$m, compatible with the excess observed in Fig. 7, where we also make use of MIR photometry.

To determine the velocity associated with the gas producing the most prominent emission features, we fit the emission profiles with a Lorentzian function, yielding a measurement of the FWHM velocity (hereafter $v_{\rm FWHM}$). We corrected the measured width of the lines by the spectral resolution to infer the value of $v_{\rm FWHM}$ (see Sect. 4.3 in Cai et al. 2018). Some of these velocities are comparable to the instrumental resolution ($\sim$400 km s^{-1} in the optical and $\sim$600–700 km s^{-1} in the NIR).

Figure 9 shows the emission features of Hβ, Hα, the [Ca II] doublets, the Ca II NIR triplet, He I λ10830, Pγ and Pβ. Each panel contains the data of one of these features (black lines) in velocity space, along with their best-fit Lorentzian profile (red lines). The $v_{\rm FWHM}$ (corrected for the spectral resolution) of each fit is listed in each panel and is also summarized in Table 10.

Comparison of the various line profile fits in the first spectrum reveals a non-negligible difference among the two prevalent Balmer lines. In particular, the Hβ feature exhibits a $v_{\rm FWHM}$ that is a factor of $\approx$2 higher than that measured for Hα, while

the Paschen lines exhibit velocities more consistent with Hβ. To explain this discrepancy with Hα, we performed pseudo-equivalent-width (pEW) measurements in order to estimate the Hα to Hβ pEW ratio. With pEW values of -53.02 Å and -18.75 Å for Hα and Hβ, respectively, we obtain a Hα to Hβ pEW ratio of 2.83. This value is fully consistent with the ratio 2.86 for case A recombination (Osterbrock 1989). The Pβ/Hβ and Pγ/Hβ ratios are high, indicating that the density is above the critical density for these high-excitation lines.

The observed velocity difference is likely due to the suppression of the red line wing by occultation effects commonly observed in stellar winds (see, e.g., Ignace 2016, and references therein). The line profiles are quite symmetric, which likely indicates optically thick lines in a homologous velocity field (Ignace 2016, see their Fig. 8). However, it is also possible that we see rotational broadening from material that was in Keplerian orbits with $v = \sqrt{\frac{GM}{r}}$, likely related to an accretion disk. If this material were ejected by a shock, it is possible that the conservation of angular momentum would lead to conservation of angular velocity. We consider this idea plausible, but suspect that the
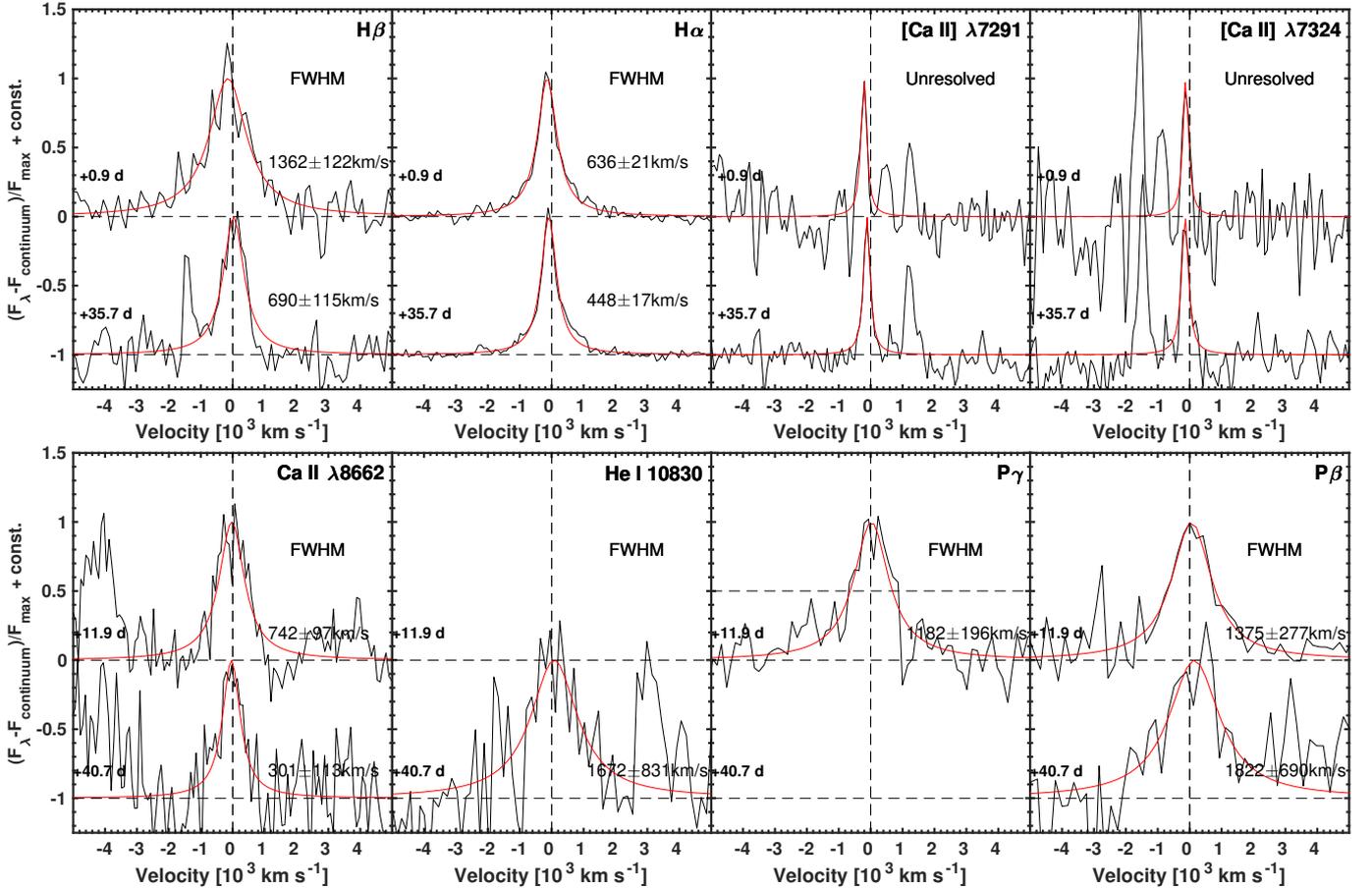
Fig. 9. Prominent spectral features identified in the spectra of SNhunt120. These include Hβ, Hα, [Ca II], the Ca II NIR triplet, He I λ10830, Pγ, and Pβ. The continuum of each spectrum was subtracted using a low-order polynomial fit to the observed data, and for presentation purposes, the peak of each line was normalized to unity. The vertical dotted lines mark the rest velocity position of each ion. Lorentzian line profile fits are overplotted as red lines, and the corresponding line velocities, corrected for the resolution, are provided in the insets and are also listed in Table 10. The forbidden [Ca II] lines are unresolved.

Table 10. FWHM velocity measurements of prominent spectral features in SNhunt120.

Phase [a] (days)	Hβ $(km\,s^{-1})$	Hα $(km\,s^{-1})$	Ca II λ8662 $(km\,s^{-1})$	He I λ10830 $(km\,s^{-1})$	Pγ $(km\,s^{-1})$	Pβ $(km\,s^{-1})$
+1	1362 ± 122	636 ± 21	⋯	⋯	⋯	⋯
+12	⋯	⋯	742 ± 97	⋯	1182 ± 196	1375 ± 277
+36	690 ± 115	448 ± 17	⋯ ⋯	⋯	⋯	⋯
+41	⋯	⋯	301 ± 113	1672 ± 831	⋯	1822 ± 690

Notes. [a]Phase with respect to date of discovery.

former of optically thick lines in a homologous flow is more probable.

We conclude here with a few words on the presence of helium. The visual wavelength spectra of SNhunt120 shown in Fig. 8 lack any discernible features associated with He I lines. However, as pointed out above, we do link a feature in the +41 d NIR spectrum of SNhunt120 to He I λ10830 (see Fig. 9). Evidence for He I lines was previously documented in a series of high-dispersion visual wavelength spectra of the ILRT NGC 300-2008-OT (Berger et al. 2009), therefore there is precedent for this, and He I λ10830 was also documented in NIR spectra of NGC 300-2008-OT (Valerin 2019). The presence of helium might indicate that a helium-rich envelope is formed through a second dredge-up phase (see Sect. 4.2.3). However,

at +40 d the T_{BB} is 6000 K (see Fig. 6, right panel), which is too cool to excite He I lines, and therefore any signatures of helium are likely due to circumstellar interaction (CSI) and not necessarily due to a high helium abundance.

3.3. Progenitor constraints

Because of the distance of SNhunt120, we cannot reach the expected magnitude level of the various progenitor types, as was done, for example, with SN 2008S (e.g., Botticella et al. 2009). In particular, the low resolution of *Spitzer* (+ IRAC) precludes any attempt of detecting the progenitor in the MIR. We searched public archives for images obtained with ground-based telescopes, but were unable to locate any suitable NIR images;
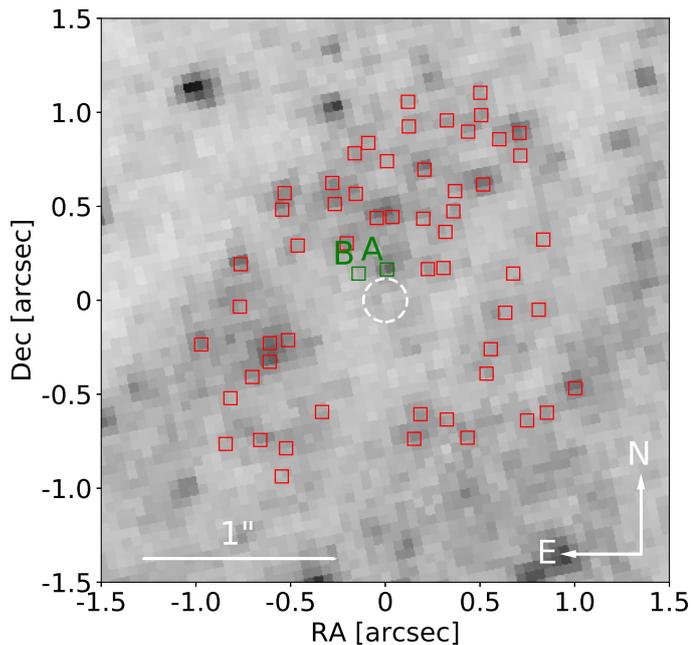
Fig. 10. Pre-explosion HST (+ ACS) F625W-band image of NGC 5775. The location of SNhunt120 in the image is highlighted with a dashed circle with a radius that corresponds to the 1-sigma positional uncertainty. No candidate sources are detected within the dashed circle down to a conservative limiting magnitude of $m_{F625W} = 27$ mag. The green squares indicated with A and B are two nearby sources discussed in the text. The red squares are all sources detected by DOLPHOT above a 3-sigma significance.

we note that UKIRT (+ WFCAM) images of NGC 5775 are too shallow to be useful.

In order to study the physics of the progenitor, we examined a set of HST (+ ACS) images taken on 21 August 2005. NGC 5775 was observed with the $F625W$ filter (approximately equivalent to Sloan r band) for 4×573 s and with the $F658N$ filter (6848 s total split across 12 exposures). To determine the location of SNhunt120 in these data, a series of 23 Swope i-band images were used to identified 17 sources om common with the HST (+ ACS) $F625W$ filter image.

We take the average of the transformed positions of SNhunt120 as determined from each of the Swope images as our best estimate of the progenitor location in the prediscovery image, which is plotted in Fig. 10. This exercise provides an x, y pixel coordinate for SNhunt120 of 3605.77 ± 2.35 and 1018.15 ± 2.29 (indicated in Fig. 10 with a dashed circle). Here the uncertainties reflect the standard deviation among the transformed positions.

Using DOLPHOT, a dedicated package for HST photometry[2], we performed PSF photometry on the F625W images. DOLPHOT detected over 50 sources above a 3-sigma significance and a single source that is somewhat consistent with the transformed location of SNhunt120. The position of sources detected with significance are indicated in Fig. 10, while the source (detected with a 17-sigma significance) nearest the expected location of SNhunt120 is also denoted with an A. Source A is offset by 3 pixels, or 0″.15 from the center of the dashed circle and has an apparent F625W magnitude of $m_{F625W} = 25.89 \pm 0.06$ in the HST flight system (VEGAMAGs). In addition, a lower significance (4.1-sigma) source is also detected 3.3 pixels from the

center of the circle and is denoted source B, with a brightness of $m_{F625W} = 27.56 \pm 0.28$ mag.

Finally, we considered the possibility that the progenitor of SNhunt120 was not detected in the ACS image. In order to determine the limiting magnitude, we selected a 4″ region surrounding the transient where the background and source density was comparable to that at the progenitor position. A comparison of the apparent $F625W$ magnitudes of the extracted sources versus their signal-to-noise ratios reveals a clear peak in the density of sources at $m_{F625W} = 27$ mag. This value was adopted as a conservative limiting magnitude. This limiting magnitude is shallower than the detection of source A, and it implicitly accounts for realistic possibilities such as two closely blended sources, or local areas of high background.

In the absence of a high-resolution image of the host NGC 5775, we cannot draw strong conclusions from this analysis. If the source denoted A is the progenitor, then it has an absolute magnitude of -4.13 ± 0.04 mag for our adopted distance and extinction. Otherwise, we set an upper limit to the progenitor absolute magnitude of $F625W > -4.7 \pm 0.3$ mag (where the uncertainty is due to distance and extinction). Additional circumstellar extinction would serve to mask the progenitor in the optical bands, and without NIR or MIR data, we are therefore unable to provide firm conclusions.

4. Discussion

4.1. Comparison of SNhunt120 to other intermediate-luminosity red transients

We plot in Fig. 11 the +0.9 d and +35.7 d visual wavelength spectra of SNhunt120 compared to a +10.5 d spectrum of AT 2017be, a +16.9 d spectrum of PTF10fqs, a previously unpublished +36 d spectrum of NGC 300-2008-OT1, and a +39.2 d spectrum of SN 2008S. All of these spectra were corrected for the Milky Way (MW) and host reddening. The spectra of these objects are broadly similar and display the same spectral features (see Sect. 3.2) at similar velocities. Inspection of Fig. 11 reveals conspicuous Hβ and Hα Balmer emission features, as well as features attributed to forbidden [Ca II] $\lambda\lambda$7291, 7324 doublet, the Ca II NIR triplet, and Ca II H&K. Some differences are apparent, however: PTF10fqs and NGC 300-OT-1 both exhibit redder continua than the other objects, and they also exhibit weaker features at the blue end of their spectra.

In Fig. 12 we compare the absolute magnitude light curves of SNhunt120 with those of M85 2006-OT1, SN 2008S, NGC 300-2008-OT1, PTF10fqs, AT 2017be, and AT 2019abn. The plotted photometry of these objects has been corrected for reddening and placed on the absolute flux scale adopting the values reported in Table 9 for total color excess and distance modulus. The majority of these events exhibit a rise to a maximum value typically within their first two weeks of evolution, and overall, they also exhibit similar light-curve decline rates post maximum. Interestingly, SNhunt120 is as bright as SN 2008S in all the optical bands. Quantitatively, from comparison of SNhunt120 to other ILRTs, we find that it is ~2 mag brighter than the faintest objects M85 2006-OT1, PTF10fqs and AT 2017be, and about a magnitude fainter than AT 2019abn (Jencson et al. 2019; Williams et al. 2020), the brightest ILRT observed to date.

A common characteristic of well-observed ILRTs, for example, SN 2008S (Botticella et al. 2009), NGC 300-2008-OT (Prieto et al. 2009; Kochanek 2011), and AT 2017be (Cai et al. 2018), and indeed the reason that they are so named, is their

---

[2] http://americano.dolphinsim.com/dolphot/
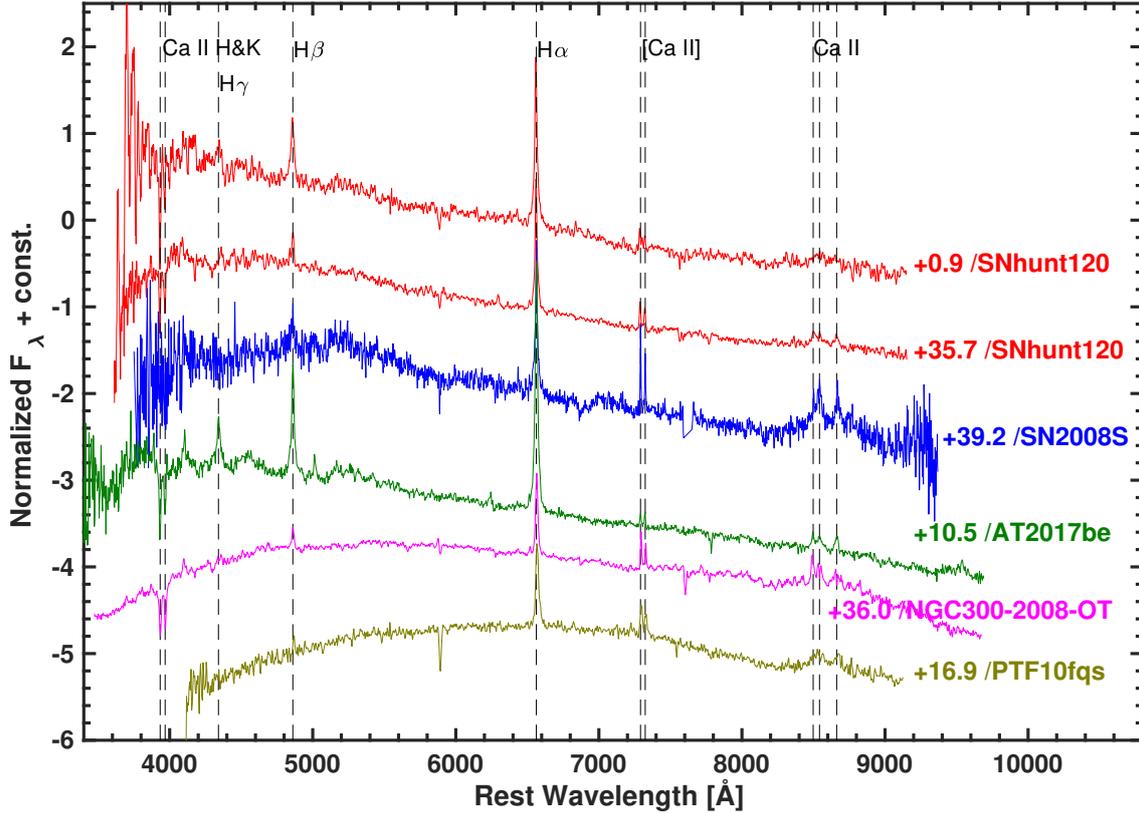
Fig. 11. Comparison of our visual wavelength spectra of SNhunt120 with similar phase (since first detection) spectra of other ILRTs. This includes AT 2017be on +10.5 d, PTF10fqs on +16.9 d, NGC 300-2008-OT1 (previously unpublished and obtained by CSP-I) on +36.0 d, and SN 2008S on +39.2 d. Each of the spectra was corrected for reddening.

emission at red wavelengths. According to Kochanek (2011), the progenitor stars that explode and give rise to these objects might be cool red supergiants of about $9\,M_\odot$, which means that they are some of the most massive AGB stars, and they are therefore referred to as super-AGB stars. Such stars are enshrouded in thick dusty stellar winds capable of absorbing even the X-rays produced from the SN shock breakout whose energy is then reemitted by the dust. These winds are so dense that dust can reform rapidly even when it is destroyed by the SN radiation field (Kochanek 2011). When they considered broadband observations of SN 2008S extending through MIR wavelengths, Botticella et al. (2009, see their Figs. 6 and 7) documented a double BB SED as early as +17.3 d after explosion. The first hot BB component reproduces emission over the optical wavelengths and is characterized by a BB temperature of $T_{\rm BB}^{\rm hot} \sim 8100\,{\rm K}$, while the second component reproduces the far-NIR through MIR emission and is characterized by $T_{\rm BB}^{\rm warm} \sim 600\,{\rm K}$.

Similarly, the *Spitzer* MIR photometry of SNhunt120 plotted in Fig. 7 also suggests a second BB component at both early and late epochs, characterized by $T_{\rm BB}^{\rm warm}$ values of $\approx 800\,{\rm K}$ and $\approx 600\,{\rm K}$, respectively. We converted the *Spitzer* $4.5\,\mu{\rm m}$ flux-point values into luminosity using our adopted distance to the host galaxy NGC 5775 (see Sect. 2.1). Using the $4.5\,\mu{\rm m}$ flux value at early times computed by interpolating from the first two *Spitzer* observations to +36.8 d, we obtain a $L_{4.5\,\mu{\rm m}}$ value of $1.2 \times 10^6\,L_\odot$, and $4.2 \times 10^5\,L_\odot$ on +1155 d. For comparison, at early times, SNhunt120 and SN 2008S exhibit similar MIR luminosity, while at late phases, SNhunt120 appears to be about three times brighter (Adams et al. 2016).

Finally, we note that the BB radius evolution of SNhunt120 is rather constant, similar to that of other ILRTs (see Fig. 4 in

Cai et al. 2019), and is not consistent with the evolution that is typically exhibited by LRNe. In LRNe, the BB radius tends to increase significantly over time (see Paper II).

4.2. Context with electron-capture supernovae

4.2.1. Comparison of UVOIR light curves of ILRTs to EC SN models

Massive stars with zero-age main-sequence (ZAMS) masses $\gtrsim 10\,M_\odot$ produce degenerate Fe-rich cores that drive the collapse of their inner cores. Depending on the ZAMS mass, such stars follow one of two paths to their demise. On one path, a neutron star is formed during core collapse, and subsequently, a supernova is produced. Alternatively, certain ZAMS mass ranges may follow a second path where their gravitational potential is so great that it is able to overcome the nuclear forces within the proto-NS core and it directly collapses into a black hole. On this second path, the entirety of the star falls back onto the BH and no supernova is produced. On the other hand, less massive stars in the range between ~ 8–$10\,M_\odot$ are expected to form degenerate oxygen-neon-magnesium (ONeMg) cores as they evolve through the super asymptotic giant branch (super-AGB) phase (see Doherty et al. 2017, for a recent review). If such ONeMg-core stars approach the Chandrasekhar mass, they may experience electron-capture reactions that induce core collapse and the production of low-luminosity electron-capture (EC) SNe (Miyaji et al. 1980; Nomoto 1984, 1987; Hillebrandt et al. 1984; Miyaji & Nomoto 1987) and neutron star remnants. An alternative hypothesis is that instead of undergoing electron-capture-induced collapse, such ONeMg-core stars could experience a
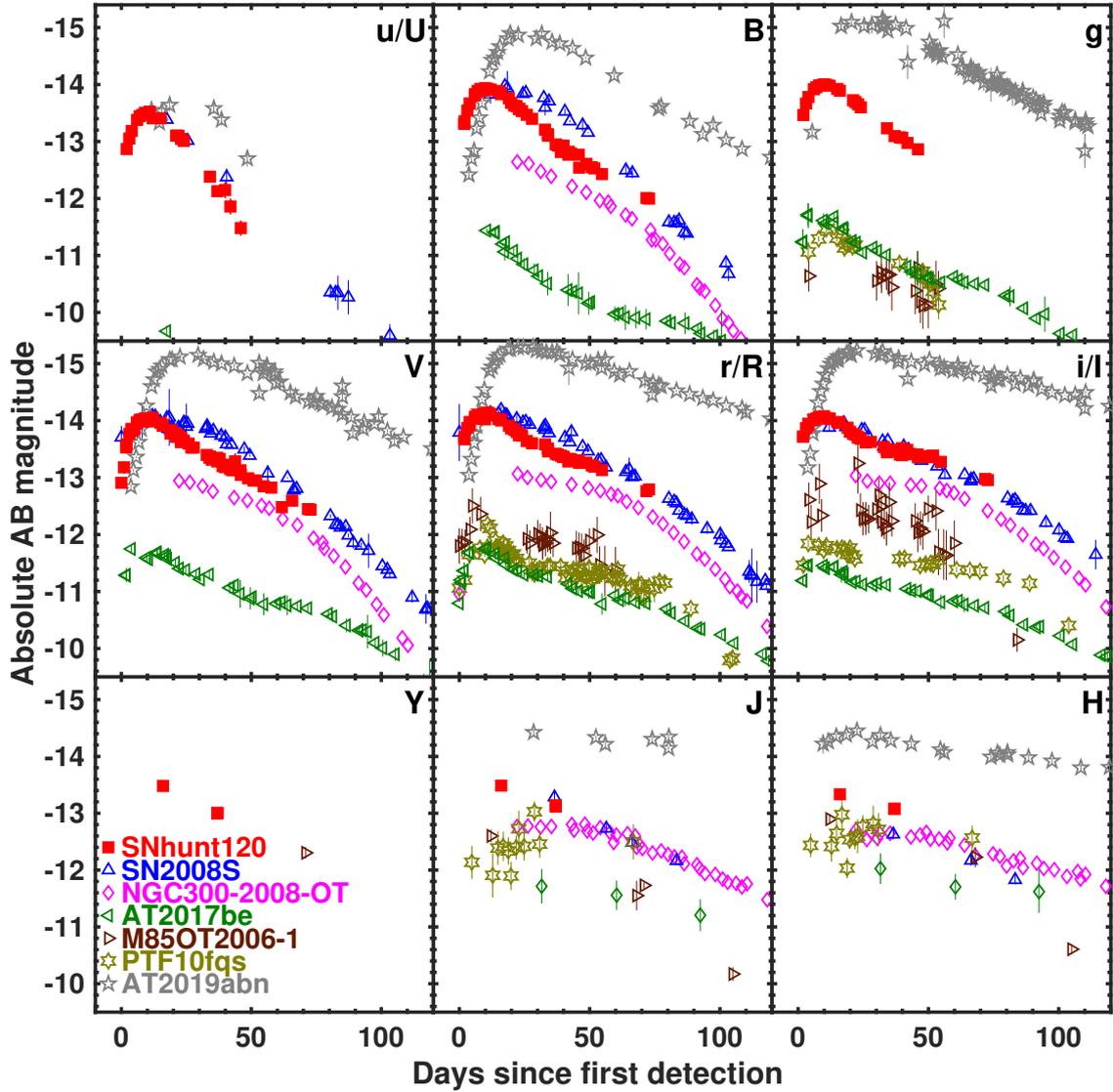
Fig. 12. Absolute magnitude light curves shifted to the AB system of SNhunt120 compared to the ILRTs M85-2006-OT1, SN 2008S, NGC 300-2008-OT1, PTF10fqs, AT 2017be, and AT 2019abn.

partial thermonuclear explosion, leading to the formation of a ONeFe white dwarf (Jones et al. 2016, 2019; Kirsebom et al. 2019; Tauris & Janka 2019).

A number of studies have suggested a link between ILRTs and EC SNe (Botticella et al. 2009; Thompson et al. 2009; Prieto et al. 2009; Pumo et al. 2009; Kawabata et al. 2010). We examine the UVOIR light curve of SNhunt120 below in relation to the comparison sample of ILRTs and to two EC SN modeled light curves that exclude and include CSI. This is followed by Sect. 4.2.2 where we present an effort to measure the expected ZAMS mass range of stars that could be the progenitors of EC SNe, followed by Sect. 4.2.3 with a short discussion of the possibility that SNhunt120 had a binary origin.

In Fig. 13 the UVOIR light curve of SNhunt120 is compared with those of our ILRT comparison sample and to synthetic light curves calculated by Moriya et al. (2014). These synthetic light curves combine the EC SN models presented by Tominaga et al. (2013) with radiative transfer calculations accounting for emission produced from CSI. It is reasonable to expect CSI to contribute to the overall energy emission budget in at least some super-AGB stars as they are commonly enshrouded in dense CSM (see Doherty 2017). We note, however, that a number

of factors influence the post-carbon burning evolution and hence the circumstellar environment, including the initial mass and the composition, the pre-explosion mass-loss history, and the core-growth efficiency (e.g., Pumo et al. 2009; Doherty et al. 2017). We therefore approach this particular comparison with caution.

Inspection of Fig. 13 reveals that consistent with the absolute-magnitude light-curve comparisons in Fig. 12, SNhunt120 lies at the bright end of the peak luminosity distribution. At peak, SNhunt120 is as bright as SN 2008S, which until the recent discovery of AT 2019abn (Jencson et al. 2019; Williams et al. 2020) was the record holder for being the brightest ILRT. Compared to the faintest ILRTs, SNhunt120 and SN 2008S are a factor of ~10 more luminous, with the added caveat that there might be even fainter ILRTs that have remained undiscovered due to selection biases. These findings follow what is demonstrated in Fig. 1, which also provides a perspective on where ILRTs and LRNe classes lie within the parameter space of peak luminosity versus decay time.

The EC SN synthetic light curve models presented by Moriya et al. (2014) that we plot in Fig. 13 (with and without CSI) reach peak luminosities of $\log_{10}(L_{\text{peak}}) \approx 42.1 \, \text{erg s}^{-1}$.
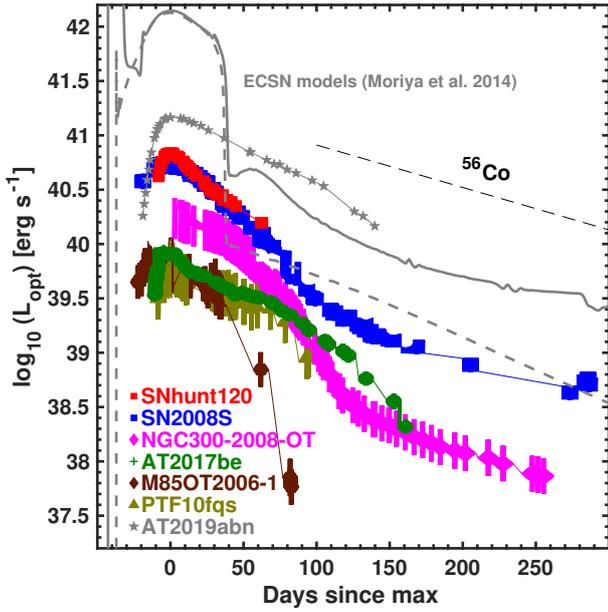
Fig. 13. Pseudo-bolometric light curve of SNhunt120 compared to the light curves of our EC SN comparison sample from Cai et al. (2018) and AT 2019abn (Jencson et al. 2019; Williams et al. 2020). The light curves of two EC SN models from Moriya et al. (2014) without CSI (dashed line) and a model with (solid line) CSI are also plotted. The dashed straight line corresponds to the complete trapping of the $^{56}Co \rightarrow$ ^{56}Fe energy deposition.

This makes them approximately a factor of ~15 brighter than SNhunt120 and SN 2008S. Although the explosion energy is predicted to be low (around 10^{50} erg) in EC SNe (Kitaura et al. 2006), the early bright luminosity in the EC SN light-curve model is caused by the extended envelope and low envelope mass found in super-AGB SN progenitors (Tominaga et al. 2013). If ILRTs are actually EC SNe, the explosion energy of EC SNe needs to be ~10^{48} erg or lower to have the lower observed peak luminosity (Tominaga et al. 2013). This in turn suggests that current EC SN explosion simulations overpredict the explosion energy. However, in principle, the envelope mass might be higher by as much as a factor of 2–3 than what was assumed in the Tominaga et al. (2013) and Moriya et al. (2014) models. If this is indeed the case, we might expect the peak luminosity to be affected, and therefore this should also be considered in future modeling efforts.

4.2.2. Mass range of EC SN progenitors

The expected range of ZAMS masses of isolated stars producing EC SNe is expected to be rather confined, and depending on metallicity, to be about $0.1-0.2\,M_\odot$ (Doherty et al. 2017, and references therein). However, within a ZAMS interval of roughly $8-11\,M_\odot$ (Jones et al. 2013, 2014; Doherty et al. 2015; Woosley & Heger 2015), the exact location of this confined parameter space for EC SN progenitors could be shifted by $1.5-2.5\,M_\odot$, depending on the metallicity and core-convective overshooting (e.g., Siess & Pumo 2006; Siess 2007; Poelarends et al. 2008).

Assuming a Salpeter initial mass function (IMF) with isolated single stars as progenitors, we can compute the expected range of ZAMS masses for the progenitors of EC SNe given the known observed fraction of 2008S-like events relative to the rate

of core-collapse SNe (10%–20%, from Thompson et al. 2009). This value is probably too high because that ILRTs and LRNe were not considered separate objects at the time of Thompson et al. (2009). If the lowest ZAMS mass to produce an EC SN is $8.5\,M_\odot$, then the highest ZAMS mass will be between 9.1 and $9.7\,M_\odot$, assuming a Salpeter IMF with isolated single stars as progenitors.

On the other hand, assuming that the lowest ZAMS mass of a progenitor star to produce an EC SN is $8.0\,M_\odot$, then the highest ZAMS mass will range between $8.6-9.1\,M_\odot$. Finally, when we assume a lower ratio of EC SNe over CC SNe, for example, 5%, as discussed in Botticella et al. (2009), the range of progenitor masses would be $8.0-8.3\,M_\odot$ or $8.5-8.8\,M_\odot$ depending on the assumption on the lowest ZAMS mass.

In a similar vein, taking the mass range of the EC SN channel from Poelarends (2007) and weighting it with a Salpeter IMF, Doherty et al. (2017) estimated that the EC SN contribution to the overall core-collapse SN rate is 5%, 17%, and 38% of all type IIP SNe for metallicities $Z = 0.02, 0.001$, and 10^{-5}, respectively, when the maximum mass for a type IIP SN is assumed to be $18\,M_\odot$, based on the analysis of SN observations by Smartt (2015). In comparison with our estimate above, we find good agreement with their result for $Z = 0.001$. These results are, however, in contrast to findings of Doherty et al. (2017). Specifically, when the results from Doherty et al. (2015) at these same metallicities were used, Doherty et al. (2017) calculated a far lower percentage of as low as 2–5% that all type IIP SNe progenitors will lead to an EC SNe. The main reason for the variation in frequency of EC SNe is due to the uncertainty in constraining the mass-loss rate of stars at low metallicity. Moreover, the EC SN candidates found in the local Universe (including SNhunt120) are all at approximately solar metallicity.

4.2.3. Binary origin for SNhunt120?

It has previously been demonstrated that the width of the initial mass range for producing EC SNe is smaller in single stars than in binary stars in nondegenerate systems (Podsiadlowski et al. 2004; Poelarends et al. 2008). The reason for this effect is that the presence in a binary can dramatically affect the structure of the core of a massive star at the time of core collapse. Stars above ~$11\,M_\odot$ are generally expected to have smaller iron cores if they lose their envelopes in a close binary. Stars in the range of $8-11\,M_\odot$ may explode as EC SNe if they are located in a close binary, while stars in wide binaries or single stars will experience a second dredge-up phase and are more likely to end their evolution as ONeMg white dwarfs. Podsiadlowski et al. (2004) argued that the minimum initial mass of a massive single star that becomes a neutron star may be as high as $10-12\,M_\odot$, while for close binaries, this mass may be as low as $6-8\,M_\odot$. These critical masses depend on the applied input physics. This includes the treatment of convection, the amount of convective overshooting, and the metallicity of the star, and will generally be lower for larger amounts of convective overshooting and lower metallicity (Podsiadlowski et al. 2004; Siess & Pumo 2006).

Although a large portion of main-sequence massive stars are found in close binaries (Sana et al. 2012), the hydrogen-rich spectra of SNhunt120 point to an isolated, or wide-orbit, progenitor star. In contrast, SN Ibn progenitors have lost their hydrogen (and also part of their helium) envelopes and are embedded in dense helium-rich CSM, giving rise to narrow helium spectral features that appear in visual wavelength spectra (e.g., Hosseinzadeh et al. 2017).

5. Conclusion

We have added to the growing populations of intermediate-luminosity red transients (ILRTs). Here in Paper I we considered SNhunt120, a gap transient discovered within days of its inferred explosion epoch that exhibits many observational properties consistent with those of other well-studied ILRTs, including an MIR excess extending from early to late phases. Reaching an *r*-band peak magnitude of −15.05 mag and exhibiting a decay time of 44 days, SNhunt120 is one of the brightest and fastest evolving ILRTs observed to date (see Fig. 1). Furthermore, comparison of the UVOIR light curves of SNhunt120 and other ILRTs to current electron-capture SN simulations reveals that the models overpredict the explosion energy. This should be considered in future modeling efforts. In Paper II we present a detailed examination of the luminous red nova designated AT 2014ej.

References

Adams, S. M., Kochanek, C. S., Prieto, J. L., et al. 2016, MNRAS, 460, 1645
Baltay, C., Rabinowitz, D., Hadjiyska, E., et al. 2013, PASP, 125, 683
Berger, E., Soderberg, A. M., Chevalier, R. A., et al. 2009, ApJ, 699, 1850
Berger, E., Marion, G.H., Hsiao, E., Foley, R., & Chornock, R. 2012, ATel., 4009
Blagorodnova, N., Kotak, R., Polshaw, J., et al. 2017, ApJ, 834, 107
Bond, H. E. 2018, Res. Notes Am. Astron. Soc., 2, 176
Bond, H. E., Bedin, L. R., Bonanos, A. Z., et al. 2009, ApJ, 695, L154
Botticella, M. T., Pastorello, A., Smartt, S. J., et al. 2009, MNRAS, 398, 1041
Cai, Y. Z., Pastorello, A., Fraser, M., et al. 2018, MNRAS, 480, 3424
Cai, Y.Z., Pastorello, A., Fraser, M., et al. 2019, A&A, 632, L6
Cid Fernandes, R., Mateus, A., Sodré, L., Stasińska, G., & Gomes, J. M. 2005, MNRAS, 358, 363
Contreras, C., Phillips, M. M., Burns, C. R., et al. 2018, ApJ, 859, 24
Doherty, C. L., Gil-Pons, P., Siess, L., Lattanzio, J. C., & Lau, H. H. B. 2015, MNRAS, 446, 2599
Doherty, C. L., Gil-Pons, P., Siess, L., & Lattanzio, J. C. 2017, PASA, 34, e056
Filippenko, A. V. 1997, ARA&A, 35, 309
Fitzpatrick, E. L. 1999, PASP, 111, 63
Hamuy, M., Folatelli, G., Morrell, N. I., et al. 2006, PASP, 118, 2
Hashimoto, M., Iwamoto, K., & Nomoto, K. 1993, ApJ, 414, L105

Hillebrandt, W., Nomoto, K., & Wolff, R. G. 1984, A&A, 133, 175
Hosseinzadeh, G., Arcavi, I., Valenti, S., et al. 2017, ApJ, 836, 158
Howerton, S., Prieto, J., & Drake, A.J. 2012, ATel., 4004
Hsiao, E. Y., Phillips, M. M., Marion, G. H., et al. 2019, PASP, 131, 014002
Humphreys, R. M., Bond, H. E., Bedin, L. R., et al. 2011, ApJ, 743, 118
Ignace, R. 2016, Adv. Space Res., 58, 694
Jencson, J. E., Adams, S. M., Bond, H. E., et al. 2019, ApJ, 880, L20
Jones, S., Hirschi, R., Nomoto, K., et al. 2013, ApJ, 772, 150
Jones, S., Hirschi, R., & Nomoto, K. 2014, ApJ, 797, 83
Jones, S., Röpke, F. K., Pakmor, R., et al. 2016, A&A, 593, A72
Jones, S., Röpke, F. K., Fryer, C., et al. 2019, A&A, 622, A74
Kashi, A., & Soker, N. 2016, Res. Astron. Astrophys., 16, 99
Kashi, A., Frankowski, A., & Soker, N. 2010, ApJ, 709, L11
Kasliwal, M. M. 2011, PhD Thesis, California Institute of Technology, USA
Kasliwal, M. M., Kulkarni, S. R., Arcavi, I., et al. 2011, ApJ, 730, 134
Kawabata, K. S., Maeda, K., Nomoto, K., et al. 2010, Nature, 465, 326
Kirsebom, O. S., Jones, S., Strömberg, D. F., et al. 2019, Phys. Rev. Lett., 123, 262701
Kitaura, F. S., Janka, H.-T., & Hillebrandt, W. 2006, A&A, 450, 345
Kochanek, C. S. 2011, ApJ, 741, 37
Kochanek, C. S., Szczygieł, D. M., & Stanek, K. Z. 2012a, ApJ, 758, 142
Kochanek, C. S., Khan, R., & Dai, X. 2012b, ApJ, 759, 20
Krisciunas, K., Contreras, C., Burns, C. R., et al. 2017, AJ, 154, 211
Kulkarni, S., & Kasliwal, M. M. 2009, in Astrophysics with All-Sky X-Ray Observations, eds. N. Kawai, T. Mihara, M. Kohama, & M. Suzuki, 312
Kulkarni, S. R., Ofek, E. O., Rau, A., et al. 2007, Nature, 447, 458
Lipunov, V. M., Blinnikov, S., Gorbovskoy, E., et al. 2017, MNRAS, 470, 2339
López Fernández, R., Cid Fernandes, R., González Delgado, R. M., et al. 2016, MNRAS, 458, 184
Makarov, D., Prugniel, P., Terekhova, N., Courtois, H., & Vauglin, I. 2014, A&A, 570, A13
Mauerhan, J. C., Van Dyk, S. D., Johansson, J., et al. 2018, MNRAS, 473, 3765
Miyaji, S., & Nomoto, K. 1987, ApJ, 318, 307
Miyaji, S., Nomoto, K., Yokoi, K., & Sugimoto, D. 1980, PASJ, 32, 303
Moriya, T. J., Tominaga, N., Langer, N., et al. 2014, A&A, 569, A57
Nomoto, K. 1984, ApJ, 277, 791
Nomoto, K. 1987, ApJ, 322, 206
Ohsawa, R., Sakon, I., Onaka, T., et al. 2010, ApJ, 718, 1456
Osterbrock, D. 1989, Astrophysics of Gaseous Nebulae and Active Galactic Nuclei (Mill Valley, CA: University Science Books)
Pastorello, A., & Fraser, M. 2019, Nat. Astron., 3, 676
Pastorello, A., Zampieri, L., Turatto, M., et al. 2004, MNRAS, 347, 74
Pastorello, A., Della Valle, M., Smartt, S., et al. 2007, Nature, 449, E1
Pastorello, A., Mason, E., Taubenberger, S., et al. 2019, A&A, 630, A75
Pettini, M., & Pagel, B. E. J. 2004, MNRAS, 348, L59
Phillips, M. M., Simon, J. D., Morrell, N., et al. 2013, ApJ, 779, 38
Phillips, M. M., Contreras, C., Hsiao, E. Y., et al. 2019, PASP, 131, 014001
Pilyugin, L. S., Vílchez, J. M., & Contini, T. 2004, A&A, 425, 849
Podsiadlowski, P., Langer, N., Poelarends, A. J. T., et al. 2004, ApJ, 612, 1044
Poelarends, A. J. T. 2007, PhD Thesis, Utrecht University
Poelarends, A. J. T., Herwig, F., Langer, N., & Heger, A. 2008, ApJ, 675, 614
Prieto, J. L., Kistler, M. D., Thompson, T. A., et al. 2008, ApJ, 681, L9
Prieto, J. L., Sellgren, K., Thompson, T. A., & Kochanek, C. S. 2009, ApJ, 705, 1425
Pumo, M. L., Turatto, M., Botticella, M. T., et al. 2009, ApJ, 705, L138
Rau, A., Kulkarni, S. R., Law, N. M., et al. 2009, PASP, 121, 1334
Sana, H., de Mink, S. E., de Koter, A., et al. 2012, Science, 337, 444
Schlafly, E. F., & Finkbeiner, D. P. 2011, ApJ, 737, 103
Schlegel, E. M. 1990, MNRAS, 244, 269
Schlegel, D. J., Finkbeiner, D. P., & Davis, M. 1998, ApJ, 500, 525
Siess, L. 2007, A&A, 476, 893
Siess, L., & Pumo, M. L. 2006, Mem. Soc. Astron. It., 77, 822
Smartt, S. J. 2015, PASA, 32, e016
Smith, N., Ganeshalingam, M., Chornock, R., et al. 2009, ApJ, 697, L49
Smith, N., Li, W., Silverman, J. M., Ganeshalingam, M., & Filippenko, A. V. 2011, MNRAS, 415, 773
Smith, N., Andrews, J. E., Van Dyk, S. D., et al. 2016, MNRAS, 458, 950
Stritzinger, M. D., Taddia, F., Fraser, M., et al. 2020, A&A, 639, A104 (Paper II)
Tauris, T. M., & Janka, H.-T. 2019, ApJ, 886, L20
Thompson, T. A., Prieto, J. L., Stanek, K. Z., et al. 2009, ApJ, 705, 1364
Tominaga, N., Blinnikov, S. I., & Nomoto, K. 2013, ApJ, 771, L12
Tully, R. B., Courtois, H. M., & Sorce, J. G. 2016, AJ, 152, 50
Valerin, G. 2019, Master's Thesis, University of Padua
Van Dyk, S. D., Peng, C. Y., King, J. Y., et al. 2000, PASP, 112, 1532
Williams, S.C., Jones, D., Pessev, P., et al. 2020, A&A, 637, A20
Woosley, S. E., & Heger, A. 2015, ApJ, 810, 34

Appendix A: Host metallicity
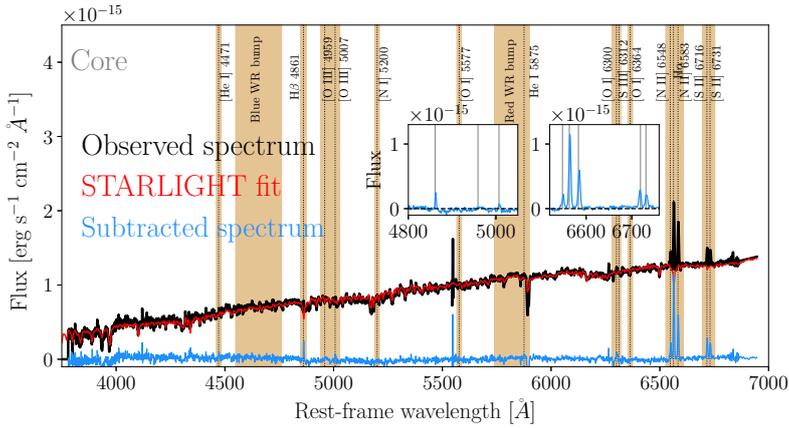
Fig. A.1. Visual wavelength spectrum of the nucleus of NGC 5775 shown in the host-galaxy rest frame (in black), and the resulting single stellar population synthesis computed by STARLIGHT (in red). The continuum-subtracted spectrum is shown in blue, where the most prominent host nebular emission features are labeled. The nebular lines shown within the insets provide flux ratios indicating a metallicity higher than solar of 8.7 ± 0.2 dex on the O3N2 scale at the core of the host. When we adopt the metallicity gradient from Pilyugin et al. (2004) of -0.47 dex R_{25}^{-1}, the metallicity at the position of SNhunt120 is estimated to be 8.34 dex. When we assume an uncertainty of 0.1 dex R_{25}^{-1} for the gradient, the uncertainty on the metallicity at the SN position would be 0.22 dex.

We plot in Fig. A.1 the SDSS spectrum of NGC 5775 and also indicate and label nebular emission lines. In particular, emission features associated with Hα, [N II] λ6584, and [S II] $\lambda\lambda$6717,6731 are labeled and fit with a single-Gaussian function in order to obtain a measure of the observed wavelength and line flux. From these features we compute an average redshift of $z = 0.00583 \pm 0.00005$.

The spectrum provides a means for estimating an oxygen metallicity abundance, but with respect to its central region. To do so, the SDSS spectrum was first fit with a modified version of STARLIGHT (Cid Fernandes et al. 2005; López Fernández et al. 2016, priv. comm.), a program that models the stellar component of the spectral continuum by estimating the fractional contribution of simple stellar populations (SSP) of different ages and metallicities, adding a dust attenuation foreground screen. The best-fit SSP model is then removed from the spectrum, and then Gaussian functions are fit to [N II] and [O III] nebular lines. From these fits we obtain a metallicity higher than solar of 8.73 ± 0.20 dex on the O3N2 scale (Pettini & Pagel 2004).

As this is an indication for the center region of the host and not for the position of SNhunt120, we extrapolated the galaxy nucleus value to the approximate location of SNhunt120 using the metallicity gradient from Pilyugin et al. (2004) of -0.47 dex R_{25}^{-1}. Adopting values for the diameter and position angle for NGC 5775 from NED and Hyperleda (Makarov et al. 2014)[3], we compute a radius-normalized distance from the host nucleus of 0.82. Altogether, we find a local oxygen abundance for SNhunt120 of $12 + \log(\text{O/H}) = 8.34 \pm 0.22$ dex, where we adopt a 0.1 dex R_{25}^{-1} uncertainty on the gradient.

Appendix B: Galactic and host reddening

NED lists the Galactic reddening along the line of sight to NGC 5775 as inferred by the Schlafly & Finkbeiner (2011) (SF11) recalibration of the Schlegel et al. (1998) infrared-based dust map to be $E(B - V)_{MW} = 0.037$ mag. When a standard $R_V^{MW} = 3.1$ value is adopted, this gives a foreground visual extinction of $A_V^{MW} = 0.115$ mag.

When estimating the host reddening of SNhunt120, we note that there are no reliable methods to do so, and regardless of the adopted method, it is accompanied by significant uncertainty. With this caveat in mind, inspection of the two low-resolution visual wavelength spectra presented below reveals a Na I D absorption feature located at the expected location given

the redshift of the host galaxy. In principle, a reliable measure of column density can provide a measure of the host extinction (e.g., Phillips et al. 2013, see their Fig. 9). Unfortunately, we are only able to estimate rough column densities from these low-dispersion spectra as they do not resolve the individual components that contribute to the absorption. Measuring the EW of the Na I feature from the low-resolution spectra indicates a value of $\text{EW}_{\text{Na I D}} \approx 2.5 \pm 0.5$ Å. This value lies outside the range of validity for the Phillips et al. (2013) relation. We next searched for evidence of a diffuse interstellar band (DIB) located at 5780 Å that is known to be correlated with A_V^{host} (Phillips et al. 2013). Unfortunately, the signal-to-noise ratio of our spectra is too low to provide any meaningful measurement of this DIB feature.

To approximately estimate the reddening of SNhunt120, we compared its observed broadband colors to the intrinsic broadband colors of other ILRTs. Fig. 5 shows that the $(V - r)$ and $(V - R)$ color evolution of the comparison sample is rather similar to that of SNhunt120. Here the broadband colors of the comparison objects were corrected for reddening using values found in the literature. When we assume that the intrinsic colors of SNhunt120 are similar to those of the bluest objects in the comparison sample, the host-galaxy color excess affecting SNhunt120 can be estimated by shifting its observed broadband colors to match the intrinsic color curves of the bluest objects in the comparison sample. In doing so, we find that the observed colors agree with the intrinsic colors of the bluest objects with $E(V - r)_{\text{host}} = 0.095 \pm 0.037$ mag. When a Fitzpatrick (1999) reddening law is adopted, this translates into a host visual extinction of $A_V^{\text{host}} = 0.64 \pm 0.25$ mag. Values exceeding those contained within the quoted uncertainty lead to poor agreement between SNhunt120 and the bluest objects in Fig. 5. When A_V^{host} is combined with A_V^{MW}, we obtain a total visual extinction of $A_V^{\text{tot}} = 0.76 \pm 0.25$ mag for SNhunt120.

Objects such as SNhunt120 are typically enshrouded by circumstellar dust, and as a result, the dust may follow a peculiar reddening law. When we consider the relations for reddening assuming graphitic (with grains of size $0.2\,\mu$m) circumstellar dust as presented by Kochanek et al. (2012b), A_λ would be 17% lower at most than that from the Fitzpatrick (1999) law in the optical (i band). If, on the other hand, the dust is formed by silicates (with grains of size $0.2\,\mu$m), A_λ would be 45% lower at most than the Fitzpatrick (1999) law in the optical (i band), and up to 30% higher in the u band.

---

[3] Hyperleda is a database of various physical properties of galaxies and can be found at http://leda.univ-lyon1.fr